SINGLE CELL MANIPULATION BY FEMTOSECOND LASERS

AND

VOLUMETRIC ANALYSIS OF CONVECTION ENHANCED DRUG DELIVERY

A Dissertation

Presented to the Faculty of the Graduate School

of Cornell University

In Partial Fulfillment of the Requirements for the Degree of

Doctor of Philosophy

by

Poornima Gadamsetty

May 2017

SINGLE CELL MANIPULATION AND OPTOPORATION USING FEMTOSECOND LASERS AND CONVECTION ENHANCED DRUG DELIVERY

Poornima Gadamsetty, Ph.D.

Cornell University 2017

Optoporation allows the minimal invasive transfer of extracellular molecules into cells. The use of a low repetition rate laser system (100 fs at 790 nm and 1 kHz repetition rate) can enable the future transfer of this technique to *in vivo* applications. However, it is essential to understand the biophysical parameter space of this technique beforehand. We examined the optoporation dependence on the extracellular calcium concentration in HeLa cells. We observed a low cell recovery rate in calcium free medium and varying cell viabilities with different calcium concentrations, possibly related to calcium dependent repair processes. Also we followed the calcium rise in the cell by a fluorescent calcium indicator. We extended our previous model of pore formation model and applied different sized dextrans to verify our assumptions on pore radius, and resealing time. Therefore, this study provides a better understanding of the biophysical processes accompanying single cell laser transfection.

Drug delivery into the brain is inhibited by the blood brain barrier and limited by the structure of the brain interstitium. Convection-enhanced delivery (CED) is a technique that delivers therapeutics by infusing directly into brain parenchyma through a needle

inserted into the brain. We developed a fast scanning, real time volumetric imaging platform to image transport of nanoparticles in the rat cortex *in vivo* with high temporal and spatial resolution and to study transport mechanisms for different sized nanoparticles in the brain interstitium and the perivascular space (PVS). Fluorescent polystyrene beads of sizes ranging from 20nm to 200nm were infused directly into a rat cortex. Particles sized >100nm had distribution routes along the perivascular spaces and were relatively hindered in the extracellular spaces in comparison to particles in the 20nm – 40nm size range that prefered transport in extracellular space. Thus, we can study the alterations in the shape, size and movement of the infusion in the brain, allowing for better control for potential clinical design and optimization.

BIOGRAPHICAL SKETCH

Poornima Gadamsetty was born on Christmas Day in a tin roofed hut in a remote village in Nagaland, a state in North East India where her father Captain (later Brigadier General) Gadamsetty Sankar was deployed battling insurgents and Gadamsetty Sita Maha Lakshmi a typical army wife who followed him everywhere. She was the second child of her parents, the elder one being her sister Bindu Gadamsetty. As an army brat she traversed the length and breadth of India moving where the young Indian Army officer got deployed. In the bargain, she has the distinction of studying in 13 schools of various hues by the time she entered 12th grade. Her high school education culminated at Army school, Wellington the seat of the prestigious Defence Service Staff College where her father was a faculty and she graduated with the highest academic standing in school history.

A young so far itinerant Poornima puts her turbulent years behind and spends the next 4 years of her life at G Narayanamma Institute of Technology And Sciences, Hyderabad graduating *magna cum laude* in her Bachelors in Instrumentation and Communication Engineering from Jawaharlal Nehru Technical University, Hyderabad, India. By now, unlike many of her age, Poornima had travelled and lived in remote places of India and had a fair idea of the societal issues and lack of infrastructure and medical facilities despite having led a sheltered life in the cantonments. This awareness and a social conscience propelled her to use her engineering skills in the medical world. Towards this end, she crossed the seven seas (as described in Indian culture) and secured admission into the highly competitive Master's program in Biomedical Engineering at

Duke University, NC. At Duke, she was a Research Assistant in Prof. Joseph A Izatts's optical coherence tomography lab and specialized in bio photonics which led to the award of Master's degree in Biomedical Engineering with specialization in Photonics. Due to her nomadic childhood, the travel bug bit her within 2 years and she moved to Cornell University to pursue her PhD in Prof Chris B. Schaffer's lab. Her 5.5 years in Schaffer's lab in particular and Cornell University in general were very educative. On one hand Schaffer's lab introduced her to a world where optics and neuroscience converge to solve several important questions in the field of single cell genetic manipulation and convection enhanced drug delivery. On the other hand she contributed to the rich fabric of campus life in Cornell University as GRF in Flora Rose Hall and ARHD at Donlon Hall. She rounded off her academic life by participating in the 14 Strings Music group and the Technology Entrepreneurship club.

She graduates with a Doctorate in Philosophy in Biomedical Engineering and minors in Neuroscience and Applied Physics in the academic field and having thoroughly absorbed the Cornell way of life.

To

Family, The Universe & Almighty

ACKNOWLEDGMENTS

I dedicate this achievement to a lot of people who helped me navigate this challenging and at times frustrating path of pursuing this degree. I have been truly blessed and fortunate to have all these people accompany me on this incredible journey. My first dedication goes to my sister, who pushed me to apply to the best of schools when no one in my family ever knew about them. I can never thank her enough for her belief in my abilities and giving me the confidence when needed. For my dad and mom I can only think of what Khalil Gibran said, “Parents are like a bow, and children like arrows. The more the bow bends and stretches, the farther the arrow flies. I fly, not because I am special, but because they stretched for me.” I thank them for battling the social conventions on my behalf and enabling me to study this far and so far.

Prof. Chris B. Schaffer is a unique person and every day is an awesome learning experience with him around. No one that I know can match his scientific prowess, legendary grant writing abilities and world famous bartending skills. In his lab I have grown both as a person and a professional. I have had the exclusive privilege of a ringside view of his journey through pre-tenure to post-tenure. The ease with which he scales greater heights would be a time tested template for all my future endeavors. I thank my committee members Prof. Joeseph Fetcho and Prof Chris Xu for their invaluable guidance and insights throughout my PhD. My collaboration with Prof. William Olbritct and Prof Xiling Shen has been one of the most rewarding experiences. I cannot express enough of my gratitude for Prof. Nozomi Nishimura, she is the glue

that holds this lab together. She has been a great teacher and a wonderful human being who eased this passage of time.

Next, I thank my wonderful lab mates, without whom things would have been utterly boring. First on the list is my undergrad, Levi Patish, whose wry humor helped me deal with fixing months of broken lasers and microscopes. Justin Rosch, my collaborator who made the PhD more rewarding. Jiahn, initially a mentee and later a good friend, has the world's best listening skills. Thanks to John Nguyen who taught me all about the lasers by saying 'just turn some sh**'. Liz with her blood pacts and throwing shade classes helped me through the cold darkness of Weill basements. Thanks to Jason Jones, I know more about hunting squirrels and deer than I need. I have to mention my broken laser support group, Sandy, Shiva, Lena and Morgan. Also this journey wouldn't have been entertaining and interesting without JC, Rob, Iryna, Calvin, Yurim, Amanda, Sungji, Mohammad and Yuting. Special mention to the most proud German I have ever met, Stefan, who flew in to Ithaca to watch Star Wars and also collaborate with me in the last phases of PhD

My deepest gratitude also extends to my friends (Kriti, Madhura, Ujjani, Anshul, John Foo, Javad, Prof. Bruce Raymond, Bailey, Nikolai, Arunima, Tanwi, Hema, Gunjan, Swati, Tushar, Sudip, Amit, Mali, Tejaswi, Nick, Avatar, Shyla, David, Colin, Basu, Uday, Bhavna, Karthik and Sonam), including members from 14 strings music group (Prof. Cliff Scherer and Tita Jane), Donlon Hall, Flora Rose Hall and Cornell's technology entrepreneurship club.

TABLE OF CONTENTS

Biographical sketch.....iii

Dedication.....iv

Acknowledgements.....v

Table of Contents.....x

List of Abbreviations.....xvi

Chapter 1. Introduction

1.1. Introduction 17

1.2. Organization 18

Chapter 2. Two Photon Microscopy and femtosecond laser based ablation

2.1. Introduction to nonlinear optical imaging 20

2.1.1 Nonlinear optical imaging 22

2.1.2 Advantages and Applications 22

2.2. Laser based ablation to manipulate biological systems 23

2.2.1. Nonlinear Ablation 23

2.2.2. Oscillator based system 25

2.2.3. Regenerative amplifier based system 26

2.3. Microscope Setup 27

2.4. Conclusion

References

Chapter 3. Optoporation: Overview

3.1. Introduction 29

3.2. Transfection Methods 30

3.3. Optoporation 31

3.4. Applications

3.5. Challenges and applications for *in vivo* single cell optoporation

3.6. Conclusion 33

References

Chapter 4. Biophysical characterization of *In vitro* optoporation

4.1. Abstract 39

4.2. Introduction 40

4.3. Methods 43

4.3.1. Cell Culture 44

4.3.2. Two-photon excitation fluorescence microscopy 44

4.3.3. Regenerative amplifier for membrane ablation 45

4.3.4. Cell labeling with Calcein AM and Oregon Green BAPTA 45

4.3.5. Model and kinetics of pore radius and resealing time 46

4.3.6. Inflow of different sized dextrans 47

4.3.7. Statistics 47

4.4. Results 48

4.4.1. Influence of Ca^{2+} concentration on cell viability during perforation 51

4.4.2. Dependence of pore radius and pore resealing time on Ca^{2+} concentration 52

4.4.3. Calcium kinetics after cell perforation 53

4.4.4. Analysis of inflow of different sized dextrans for pore size and resealing time validation 55

4.5. Discussion and Conclusion 59

References

Chapter 5. *In vivo* Optoporation

5.1. Introduction 61

5.1.1. Other *in vivo* transfection methods 63

5.1.2. Femtosecond laser based *in vivo* transfection 66

5.2. Methods 72

5.2.1. Animal Preparation 73

5.2.2. Two-photon excitation fluorescence microscopy 73

5.2.3. Regenerative amplifier for membrane ablation 74

5.2.4. Labeling and setup 74

5.3. Results

5.3.1. Astrocyte targeting and characterization through outflow analysis 75

5.3.2. Inflow analysis with shadow imaging 76

5.4. Conclusion 79

References

Chapter 6. Volumetric imaging of convection enhanced drug delivery

6.1. Abstract 83

6.2. Introduction 85

6.2.1. Perivascular and parenchymal transport 86

6.2.2. Diffusion Method 88

6.2.3. Convection Enhanced Delivery Method 90

6.3. Methods 91

6.3.1. Nanoparticle and Liposome preparation 92

6.3.2. Infusion Setup Preparation 93

6.3.3. Imaging Experiment 94

6.3.4. Image Analysis 96

6.4. Results 96

6.4.1. Particle Infusions 97

6.4.2. Larger particles Vd dependent on presence of perivascular spaces (Cloud Morphology for rigid polystyrene beads) 97

6.4.3. Volume of distribution to infusion ratio increases with particle flexibility 100

6.4.4. Cloud growth in the parenchyma decreases overtime 101

6.4.5. Perivascular spaces are more preferential as high conductance fluid pathways 121

6.4.6. Volume of distribution for larger nanoparticles is greatly influenced by perivascular spaces. 128

6.4.7. Co-Infusion of smaller and larger particles into rat cortex

6.5 Discussion and Conclusion 130

References

Chapter 7. Conclusion 136

LIST OF ABBREVIATIONS

BBB	Blood Brain Barrier
CBF	Cerebral blood flow
CBV	Cerebral blood volume
ECS	Extra cellular Space
MRI	Magnetic resonance imaging
PVS	Perivascular spaces
2PE	Two-photon excitation fluorescence microscopy
Vi	Infusate volume
Vd	Distribution Volume

CHAPTER 1

INTRODUCTION

1.1 INTRODUCTION

The unmet need to develop a single cell *in vivo* genetic optoporation system in the brain has been the foundation for this thesis. This technique has immense opportunity to address research in tumor genesis, single neuron – neuron interaction and pathogenesis of other brain diseases. Traditionally optoporation has been accomplished with high repetition rate lasers, but to manipulate deep inside the tissue and overcome optical scattering we use a low repetition rate 1kHz laser system. Therefore, we first, focus on understanding of the biophysical dynamics involved in optoporation at the *in vitro* level and then establishing of the challenging technique at the *in vivo* level.

In this dissertation, we also focus on optimizing the therapeutic potential of convection enhanced drug delivery for applications, such as treating brain tumors. Despite many advances the clinical trial success of convection enhanced drug delivery has been very limited. Literature suggests that there is need to understand the infusion and drug distribution dynamics better to be able to control, predict and optimize drug infusions via convection enhanced drug delivery. Therefore we established a platform to capture 3D volumetric images of the distribution of nanoparticles in a rat cortex in real time with convection enhanced drug delivery technique.

1.2 ORGANIZATION

Chapter 2: This chapter introduces readers to nonlinear imaging, including two photon excitation microscopy and femtosecond laser based ablation. The section on laser based ablation discusses both high and low repetition rate systems and their applicability to *in vivo* research.

Chapter 3: This chapter gives introduction to optoporation technique, including background, other transfection techniques including their disadvantages in applicability to *in vivo* systems. The current literature on *in vivo* single cell genetic manipulation is also discussed.

Chapter 4: Biophysical dynamics of single cell *in vitro* optoporation are discussed in detail in this chapter. We examined the optoporation dependence on the extracellular calcium concentration in HeLa cells. Furthermore, we extended our previous model of pore formation and applied different sized dextrans to verify our assumptions on pore radius, and resealing time. Therefore, this study provides a better understanding of the biophysical processes accompanying single cell laser transfection.

Chapter 5: Establishment of *in vivo* optoporation technique is discussed in this chapter. Furthermore, inflow and outflow experiments verify our assumptions of the feasibility

of these experiments *in vivo* and setting the stage now for future genetic, DNA plasmid transfection of a single cell *in vivo* by optoporation method.

Chapter 6: This chapter discusses volumetric imaging of convection enhanced nanoparticle delivery in rat cortex. We quantified the transport dynamics in the perivascular and parenchymal regions. Real time imaging of nanoparticle transport in the rat cortex has led to a better understanding of movement of materials that have been infused directly into brain tissue during a CED infusion. Nanoparticle size and the location of the needle tip relative to local blood vessels are both critical parameters influencing perivascular transport. By changing parameters such as particle size, the shape, size and movement of the infused particles can be altered, thus allowing for better control for potential clinical design and optimization.

Chapter 7: Conclusion chapter summarizes results and future directions from all the previous chapters. It discusses how the groundwork has been set to conduct *in* vivo single neuron optoporation and build effective CED clinical trials.

CHAPTER 2

TWO PHOTON MICROSCOPY AND LASER BASED ABLATION

Permission to reproduce **Figures 2.1, 2.3 and 2.4** was granted by Nature Publishing Group.

W. R. Zipfel, R. M. Williams, and W. W. Webb, “Nonlinear magic: multiphoton microscopy in the biosciences,” Nat. Biotechnol., vol. 21, no. 11, pp. 1369–1377, Nov. 2003.

Permission to reproduce **Figure 2.5** was granted by Applied Physics B

A. Vogel, J. Noack, G. Hüttman, and G. Paltauf, “Mechanisms of femtosecond laser nanosurgery of cells and tissues,” Appl. Phys. B, vol. 81, no. 8, pp. 1015–1047, Nov. 2005.

2.1 INTRODUCTION TO NONLINEAR OPTICAL IMAGING

In this chapter we discuss the two main technologies that have enabled me to research single cell manipulation and convection enhanced drug delivery. In the first part of this chapter we discuss two photon excitation microscopy and then move onto discuss the custom experimental setup of the two photon microscope used in these experiments. The second part of this chapter focuses on laser based ablation technique that causes nonlinear photo-damage enabling single cell manipulation both *in vitro and in vivo.*

2.1.1 Nonlinear optical imaging

Nonlinear optical imaging is a powerful tool for imaging biological systems, providing a minimally invasive way to observe their dynamics in different states. In the year 1931, it was shown[1] theoretically that absorption of multiple photons of lesser energy can produce excitation similar to that of single photon excitation. This was termed multiphoton excitation. In 1990, Denk et al. for the first time demonstrated two-photon excited fluorescence microscopy and revolutionized the field of imaging[2]. Now, two photon microscopy providing high spatial and temporal resolution, is a widely established imaging technique of fluorescence microscopy for thick tissues and live animals, involving imaging morphology, functionality, and physiology. In two photon excitation, two equal energy photons from the same laser source interacting with a fluorescent molecule can lead to excitation and emission of a single photon of

fluorescence. Jablonski diagrams for single and two photon excitation are shown in Figure 2.1, here in the case of single photon excitation, one photon is absorbed by fluorescent molecule, which reaches excited state and loses energy with emission of one photon again. However in the case of two photon excitation, two photons of equal energy are simultaneously absorbed by the fluorescent molecule for it to reach the excitation state and leads to emission of one photon only to return to the ground state. The fluorescence is generated in a localized volume in comparison to single photon excitation as shown in Figure 2.2. Here, the two photons have to be absorbed simultaneously and probability of this process occurring is quadratically dependent on the light intensity. To achieve high enough photon densities femtosecond pulsed laser systems with wavelengths in the near-IR regime are used to drive this multiphoton absorption and subsequent emission of a single photon. In multiphoton excitation, emission signal is directly proportional to the n^{th} order process of the intensity I^n. So, in two-photon excitation, the emitted fluorescent signal is proportional to I^2. Thus, absorptions occurs only in the focus where the photon density is concentrated and high enough. In contrast to confocal microscopy, excitation does not occur above and below the focal plane [2], [3].

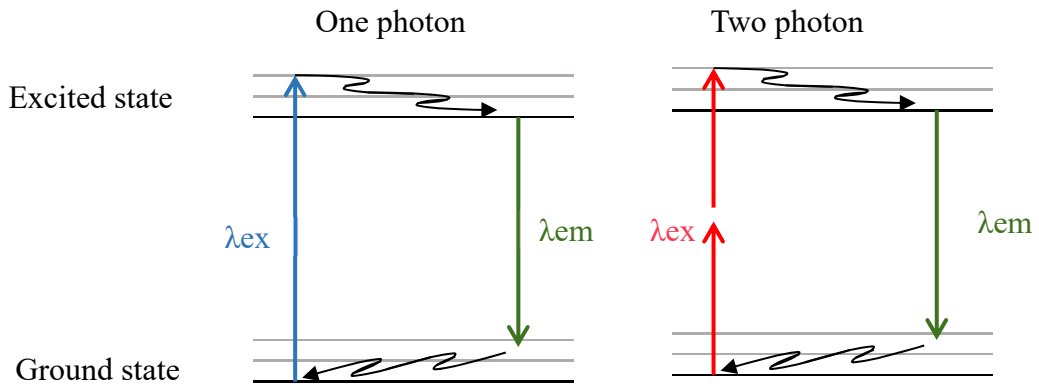

Figure 2.1 Jablonski Diagrams. One and Two photon absorption and excitation that enables fluorescence emission

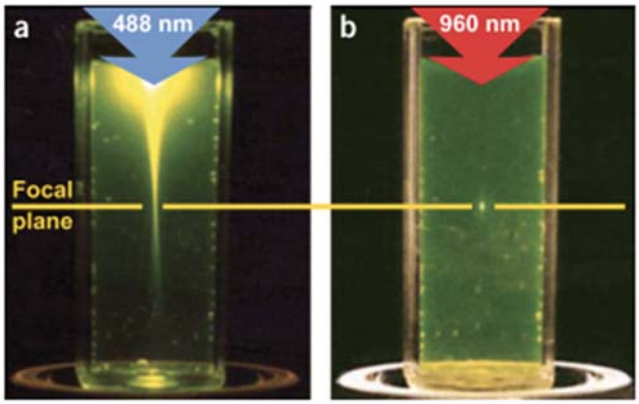

Figure 2.2 Localization of excitation by two-photon excitation. (a) Single-photon excitation of fluorescein by focused 488-nm light (0.16 NA). (b) Two-photon excitation using focused (0.16 NA) femtosecond pulses of 960-nm light.[5].

2.1.2 Advantages and Applications

Main advantages with two photon microscopy are localized excitation and extensive wavelength range for excitation of a majority of fluorophores. A majority of common fluorescent molecules and dyes can be used with this imaging, including alexa dyes, green fluorescent protein, dsRed and mCherry. By limiting excitation volume to a localized area, it achieves reduced, photobleaching and photodamage effects. All these factors together also allow higher viability of biological specimens with 3D deep imaging at high temporal and spatial resolution. Thus, establishing two photon imaging as one of the most widely used imaging tool.

Being a widely established imaging tool, many studies have utilized it in the past two decades. Figure 2.3 highlights a few applications of two photon microscopy, simultaneous excitation of different fluorophores in cells (Figure 2.3a, b) and deep imaging of calcium dynamics in the neuropil of live lobster (Figure 2.3c, d). In addition to these, it has been applied for visualizing specific classes of cells in the brain like microglia, astrocytes, neurons simultaneously and quantifying blood flow in live mouse brain [4],.

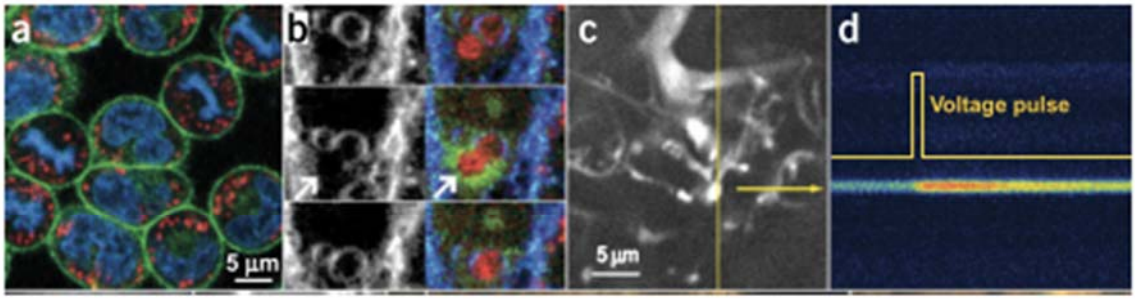

Figure 2.3 Applications (a) Simultaneous excitation and emission of three different fluorophores at 780nm in RBL-2H3 cells labeled by DAPI for DNA (blue pseudo color), TRITC for mitochondria (red) and PATMAN for plasma membrane (green). (b) Dynamic behavior of coalescing in stationary granules, with cells labeled with acridine orange for granules staining (green and red) and PATMAN for plasma membrane staining (grayscale and blue)[19]. (c) and (d) Calcium green 1 labelling to observe calcium dynamics in neuropil of lobster's motoneuron at 300um depth[20][5].

2.2 LASER BASED ABLATION TO MANIPULATE BIOLOGICAL SYSTEMS

Besides imaging of biological systems, femtosecond laser system has also been used for subsurface micromachining and nanostructuring of non-biological transparent materials[6][7]. In the past decade, this technology has advanced to manipulate biological systems by laser based ablation of cells, neurons and blood vessels. Its ability for precise and controlled ablation makes it ideal for dynamic manipulation of biological systems, understanding disease propagation, genetic manipulation and generation of both acute and chronic animal models[8][9][10][11][12].

2.2.1 Nonlinear Ablation

To induce ablative damage higher peak intensities are needed. Optical breakdown threshold of water has peak intensities of the order of 10^{13} W/cm^2 [13]. At such high intensities, photons have a higher probability of ionization and transferring energy. At the focal volume, multi-photon ionization excites electrons from ground state to the state of ionization or conduction band

Another process contributing here is the inverse bremsstrahlung absorption (IBA)[15][16]. In IBA free electrons absorb photons non-resonantly from the applied laser field. These electrons cause impact ionization of the surrounding atoms and result in more semi free electrons that in turn cause more impact ionization and so on. On reaching a threshold, avalanche-ionization or avalanche-breakdown[13] occurs and produce sufficient plasma density that contributes towards damaging the material[15] [16]. This is further illustrated in Figure 2.5.

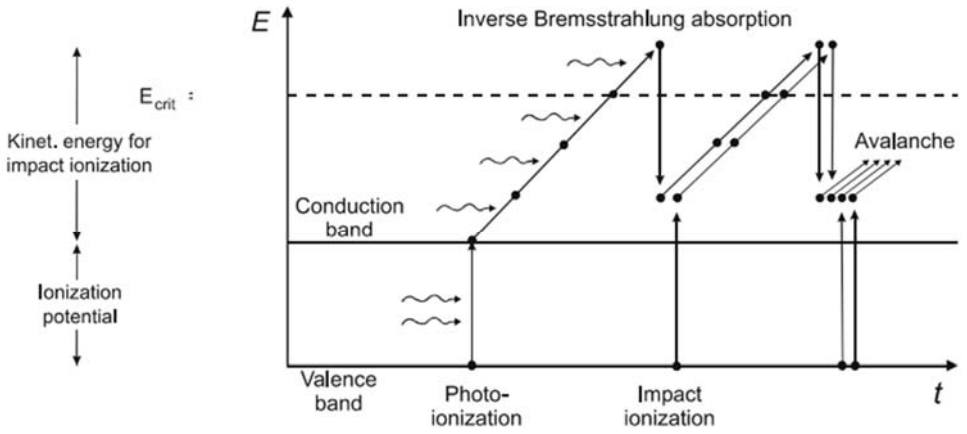

Figure 2.5 Photoionization, inverse Bremsstrahlung absorption, impact and avalanche ionization are shown here in the process of formation of plasma that subsequently leads to photo disruption[13]

As light passes deeper into tissue, only the unscattered light on reaching the focal volume can drive non-linear absorption and subsequent damage. However, increase in tissue depth leads to an exponential decrease in the fraction of unscattered light reaching the sub micrometer-sized focal volume. In the next section we compare two systems that introduce nonlinear process for ablation in biological systems: Oscillator system and Regenerative amplifier laser system. We compare two systems here because we need a system that has an advantage of overcoming scattering losses and driving nonlinear absorption in thick and deeper tissues. This is a major requirement for *in vivo* applications. In this thesis, the goal is to apply this technique in live rodent neocortex *in vivo* and characterizing it by manipulation of Hela cells *in vitro*.

2.2.2 Oscillator based system – Thermal damage

This system is a 80MHz high repetition rate Ti:sapphire laser at pulse intensities of about of 10^{11} W/cm^2. This is below the optical break down threshold and just above the pulse energies used for nonlinear imaging. Here, at the focal volume a low density electron plasma is formed that releases free electrons causing disruption of chemical bonds, potential accumulative localized heating to increase membrane permeability or other targeted sample damage [13][10]. To overcome losses due to tissue scattering at larger depths, the average power of the laser would have to be increased, but in high repetition rate laser systems, thermal damage could occur due to the considerably larger average laser power. To reach even sufficient high intensity to cause membrane

disruption just a few microns below the surface of the tissue sample, average power could be in the order of a watt. This linear absorption can lead to tissue damage even outside the focal region.

2.2.3 Regenerative Amplifier based system – Nonlinear Damage

In this system, we use a low repetition rate 1kHz Ti:Sapphire laser with peak intensities of 10^{15} W/cm^2, which is well above the optical breakdown threshold for water. At these rates, it has high pulse energy and lower average output power A single pulse is capable of driving nonlinear multiphoton ionization and avalanche ionization within the sample, producing high density plasma at the focus[17]. These together produce thermoelastic stress that in turn create transient nanometer and micron sized cavitation bubbles, which lead to cell membrane dissection in nanoscale range or other targeted sample damage [13][15][16]. In *in vivo* applications, to overcome optical scattering and to go deeper into the tissues higher energy pulses will be needed. Since, repetition rate is in the kHz range, average power being delivered deep into the tissue is in the order of mill watt and this eliminates the potential for thermal damage.

2.3 MICROSCOPE SETUP

The experimental setup described in this section is the setup used for all the experiments in this thesis. A custom designed two photon microscope was used for imaging along with a low-energy, 100 fs, 800 nm, 76 MHz repetition rate Ti:Sapphire

oscillator (Mira-HP; Coherent), pumped by a continuous wave diode-pumped solid state laser (Verdi-V18; Coherent). For ablation, the laser used was a 50 fs, 800 nm, 1 kHz repetition rate, Ti:Sapphire regenerative amplifier (Legend 1k USP; Coherent) pumped by a Q-switched laser (Evolution 15; Coherent) and seeded by a Ti:sapphire oscillator (Chinhook Ti:sapphire laser; Kapteyn-Murnane Laboratories Inc., pumped by Verdi-V6; Coherent, Inc.). For the experiments in this thesis, both two channel and four channel custom built two photon microscopes were used. Figure 2.4 illustrates a standard setup[5] of two channels for a multiphoton microscope.

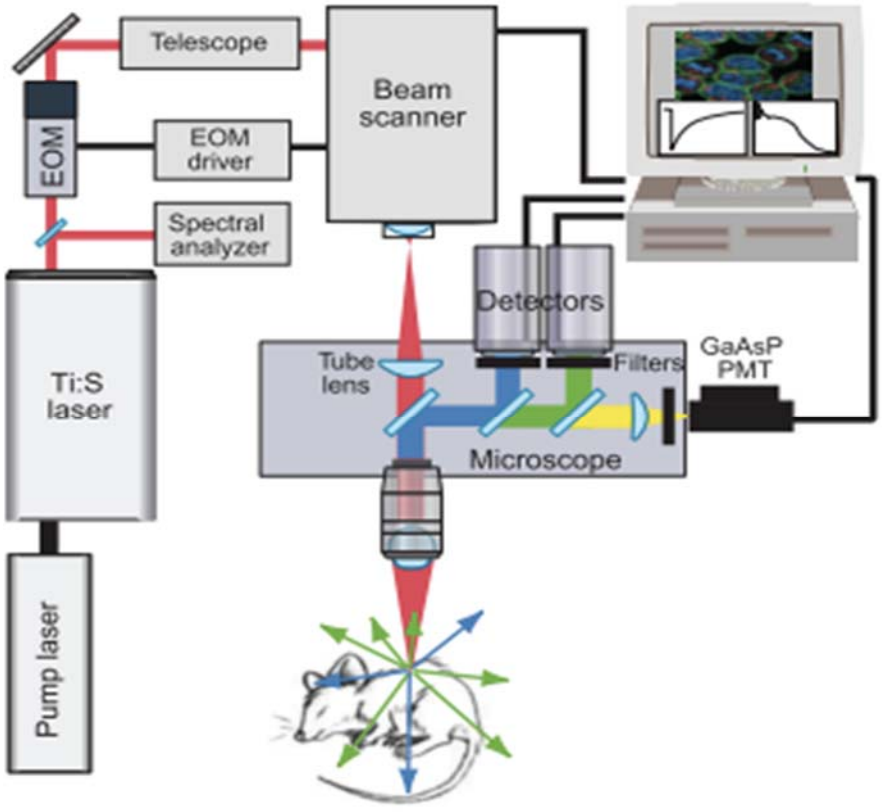

Figure 2.4 Schematic of a standard multiphoton microscope system[5].

The microscope optical paths were all custom built. Beams are first routed through a series of telescope and dispersion compensating prisms. This optical setup is such that the beam size is large enough to just overfill the back aperture of the objective. Since the beam profile is Gaussian, overfilling ensures optimal resolution with maximum power transmission. X-Y galvanometer scanners (6230H, Cambridge Technology) were used for implanting fast laser scanning over the sample and their rotation determined the field of view. The galvanometer parameters are controlled by software. These scanners can determine both spatial and temporal resolution. Immediately after the scanners, a polarizing beam splitter is used to focus imaging and ablation beam onto the same plane to allow simultaneous imaging and targeting. For precise laser based ablation, additional control of ablation pulse energy is required. This was achieved by using neutral density filters and a mechanical shutter with a 2 ms minimum opening time (VMM-D4; Uniblitz). Post imaging beam excitation, emitted light from the fluorescent sample passed through a set of dichroic filters. These filters are used for directing components of the emitted light into their respective wavelength appropriate channels. Then, each channel leads? to a photo multiplier tube to get a voltage output. The voltage output is further amplified, digitized and recorded using ScanImage (r3.8.1, Janelia Farm, USA). Image analysis and processing used custom written scripts in MATLAB (The MathWorks, Natick, MA) and ImageJ.

2.4 CONCLUSION

On comparison of both oscillator and regenerative amplifier systems, their transfection efficiencies were comparable at about 45% [18]. In this thesis we use low repletion rate laser or even 1-2 pulses to maintain very low average laser powers while having higher pulse energy (11-14nJ) to drive nonlinear absorption at larger depths up to 300-500 microns. It has not been fully characterized and explored in single cell manipulation both *in vitro* and *in vivo*. In this thesis, the goal is to characterize this ablative mechanism to be able manipulate single cells in live rodent cortex. This is capable of being a very useful tool to dynamically manipulate and study functionality and diseases *in vivo*.

REFERENCES

[1] M. Göppert-Mayer, “Uber elementarakte mit zwei quantensprüngen,” *Ann. Phys*, pp. 273–294, 1931.

[2] W. Denk, J. Strickler, and W. Webb, “Two-photon laser scanning fluorescence microscopy,” *Science (80-.).*, vol. 248, no. 4951, pp. 73–76, Apr. 1990.

[3] F. Helmchen and W. Denk, “Deep tissue two-photon microscopy.,” *Nat. Methods*, vol. 2, no. 12, pp. 932–40, Dec. 2005.

[4] C. B. Schaffer *et al.*, “Two-photon imaging of cortical surface microvessels reveals a robust redistribution in blood flow after vascular occlusion,” *PLoS Biol.*, vol. 4, no. 2, pp. 258–270, 2006.

[5] W. R. Zipfel, R. M. Williams, and W. W. Webb, “Nonlinear magic: multiphoton microscopy in the biosciences,” *Nat. Biotechnol.*, vol. 21, no. 11, pp. 1369–1377, Nov. 2003.

[6] C. B. Schaffer, A. Brodeur, J. F. García, and E. Mazur, “Micromachining bulk glass by use of femtosecond laser pulses with nanojoule energy,” *Opt. Lett.*, vol. 26, no. 2, p. 93, Jan. 2001.

[7] F. Korte *et al.*, “Towards nanostructuring with femtosecond laser pulses,” *Appl. Phys. A*, vol. 77, no. 2, pp. 229–235.

[8] N. L. Rosidi *et al.*, “Cortical microhemorrhages cause local inflammation but do not trigger widespread dendrite degeneration.,” *PLoS One*, vol. 6, no. 10, p. e26612, Jan. 2011.

[9] N. Nishimura, C. B. Schaffer, B. Friedman, P. S. Tsai, P. D. Lyden, and D. Kleinfeld, “Targeted insult to subsurface cortical blood vessels using ultrashort laser pulses: three models of stroke.,” *Nat. Methods*, vol. 3, no. 2, pp. 99–108, Feb. 2006.

[10] A. A. A. Davis, M. J. J. Farrar, N. Nishimura, M. M. M. Jin, and C. B. B. Schaffer, “Optoporation and genetic manipulation of cells using femtosecond laser pulses.,” *Biophys. J.*, vol. 105, no. 4, pp. 862–71, Aug. 2013.

[11] I. V Il’ina, A. V Ovchinnikov, O. V Chefonov, D. S. Sitnikov, M. B. Agranat, and A. S. Mikaelyan, “Noncontact microsurgery of cell membranes using femtosecond laser pulses for optoinjection of specified substances into cells,” *Quantum Electron.*, vol. 43, no. 4, pp. 365–369, Apr. 2013.

[12] I. V Il’ina, A. V Ovchinnikov, D. S. Sitnikov, O. V Chefonov, and M. B. Agranat, “Noncontact microsurgery and delivery of substances into stem cells by means of femtosecond laser pulses,” *Quantum Electron.*, vol. 44, no. 6, pp. 594–598, Jun. 2014.

[13] A. Vogel, J. Noack, G. Hüttman, and G. Paltauf, “Mechanisms of femtosecond laser nanosurgery of cells and tissues,” *Appl. Phys. B*, vol. 81, no. 8, pp. 1015–1047, Nov. 2005.

[14] G Mainfray and G Manus., “Multiphoton ionization of atoms.,” *Reports Prog. Phys.*, vol. 54, p. 1333, 1991.

[15] A. V. and V. Venugopalan, “Mechanisms of Pulsed Laser Ablation of Biological Tissues,” *Chem. Rev.*, pp. 577–644, 2003.

[16] C. Schaffer, N. Nishimura, E. Glezer, A. Kim, and E. Mazur, “Dynamics of femtosecond laser-induced breakdown in water from femtoseconds to microseconds,” *Opt. Express*, vol. 10, no. 3, p. 196, Feb. 2002.

[17] C. Schaffer, N. Nishimura, E. Glezer, A. Kim, and E. Mazur, “Dynamics of femtosecond laser-induced breakdown in water from femtoseconds to microseconds,” *Opt. Express*, vol. 10, no. 3, p. 196, Feb. 2002.

[18] A. A. Davis, M. J. Farrar, N. Nishimura, M. M. Jin, and C. B. Schaffer, “Optoporation and genetic manipulation of cells using femtosecond laser pulses.,” *Biophys. J.*, vol. 105, no. 4, pp. 862–71, Aug. 2013.

[19] R. M. Williams and W. W. Webb, “Single granule pH cycling in antigen-induced mast cell secretion,” *J. Cell Sci.*, vol. 113, no. 21, 2000.

[20] P. Kloppenburg, W. R. Zipfel, W. W. Webb, and R. M. Harris-Warrick, “Highly localized Ca(2+) accumulation revealed by multiphoton microscopy in an identified motoneuron and its modulation by dopamine.,” *J. Neurosci.*, vol. 20, no. 7, pp. 2523–33, Apr. 2000.

CHAPTER 3

OPTOPORATION: AN OVERVIEW

3.1 INTRODUCTION

Mammalian cells are impermeable to most macromolecules. A very critical technique in biomedical research is transfection, which is the introduction of foreign exogenous material into a cell. To genetically modify a cell efficiently, transfection needs to be highly precise and controlled. The use of focused ultrashort laser pulses to transiently perforate a cell membrane to introduce exogenous foreign genetic material into the cell, is termed as optoporation. In the past decade, a lot of studies have used femtosecond lasers to genetically **and functionally** manipulate a wide variety of cells *in vitro*. In this chapter, we will discuss various transfection techniques currently being used, laser based transfection and advancements in the field of optoporation.

3.2 TRANSFECTION METHODS

Transfection methods can be classified under chemical, viral and physical methods[1]. Figure 3.1 illustrates different methods for transfection including optoporation. In this section we cover a few of these techniques. . Optoporation can be applied both to a bulk of cells simultaneously, or in more cell-targeted fashion by applying the electric field locally through, for example, a patch pipette. .One of the physical methods is Electroporation, which involves application of electric field to induce disturbance in the phospholipid bilayer of cell membrane. This causes formation of hydrophilic pores through which exogenous material enters the cell. It is a highly efficient system and has a wide range of application, including automated *in vitro* cell-

targeted and robotic electroporation system with transfection rates of 2 cells/min and study of calcium induced tumor necrosis[2]–[4]. It has also been applied for single cell *in vivo* targeting in combination with a variety of other techniques including patch clamp and shadow imaging[5]–[8].

In sonoporation ultrasound induces cell permeabilization by cavitation of microbubbles [9]. Microbubbles are small structures filled with gas and stabilized by either a protein, lipid or polymer shell. Ultrasound pressure waves can easily compresses them causing cavitation effect, which in turn implode for cell permeabilization to occur. Studies include sonoporation mediated uptake of peptides, low molecular weight drugs and genetic material (pDNA, mRNA) [10]. Most previous work is limited to *in vitro* studies as, for *in vivo* single cell manipulation, sonoporation has challenges of low cell viability and throughput, as well as physical and technical limitations.

Microinjection is another highly invasive technique that involves using a glass pipette to enter the cell membrane and directly transfer external molecules. Its application is also very limited *in vivo* due to its highly invasive nature [11]. Microinjection is also limited by low viability of cells, throughput and by being physically challenging. Another widely used method is transfection by viral vectors, which target a region or specific type of cells both *in vtro* and *in vivo*. However, the size of DNA that can delivered by viral constructs is limited, affecting specificity and expression level for a single cell. Viral gene delivery technique when applied *in vivo*, generally affect bulk volume of cells based on their anatomical location or functionality,

but they have little to limited selectivity for single cell. To circumvent this problem there have been studies using retroviral and lentiviral vectors to have multicolor RGB labeling a larger population of neurons, where a specific hue determines each individual cell [12].

Chemical methods include lipid mediated and polymer based (calcium phosphate) transfection. In polymer based transfection, the underlying principle is attraction of positively charged nucleic acid - chemical complexes with negatively charged cell membrane and delivered through endocytosis/phagocytosis. Similarly in lipid based transfection method, cationic lipid reagent forms complexes with nucleic acid and are endocytosed by the cell to be released into the cytoplasm. Once in the cytoplasm, transfected DNA genetic material is translocated into the nucleus for expression. However, these methods have a drawback for applicability to *in vivo* systems mainly due to their high dependence on cell type and culture conditions [13].

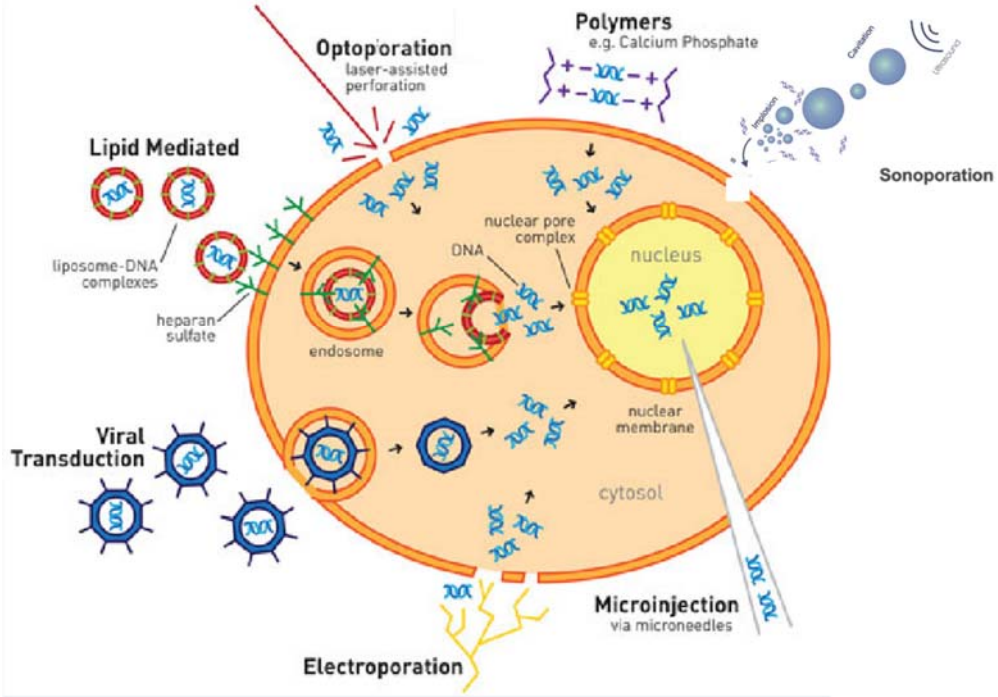

Figure 3.1 Schematic diagram of various transfection methods. Adapted from reference [42]

Several methods have been used for transfection, but they are limited in their application for targeted transfection of a single cell *in vivo* such as genetic manipulation of a single cell in live rodent cortex. A minimally invasive technique for single cell genetic manipulation could probably open many opportunities for research. Brain tumors, like glioblastoma can be investigated at initial cellular level by transfecting oncogenes into a single targeted astrocyte *in vivo*. This will drive tumor development into targeted cells and will allow *in vivo* imaging of the earliest stages of tumor growth and of the cellular interactions that facilitate or, perhaps more interestingly, arrest tumor development. We can uniquely study functional connectivity of cortical neuronal circuits, by transfecting light-gated ion channels into a single neuron. Thus, this new

capability will allow us to investigate cell-cell interactions and early stages of genetically driven diseases, all *in vivo*.

3.3 OPTOPORATION

The phenomenon of laser based transfection was first discovered by Tsukakoshi et al. in 1984 [14]. They focused a nanosecond pulsed laser at 335 nm on normal rat kidney cells in a bath solution of plasmid DNA. The cells got transfected days later. In the past two decades, optoporation has been demonstrated by a variety of lasers ranging from continuous wave to pulsed infrared and transfection efficiencies vary with laser type. In 2002, Tirlapur et al. demonstrated that using femtosecond laser pulses resulted in higher transfection efficiency and viability in mammalian cells [15]. Vogel et al. investigated the mechanisms of femtosecond laser based optoporation. In continuous wave (CW) laser based optoporation, localized heating of the plasma membrane drives transfection. However, optoporation with femtosecond laser at high repetition rates generates a low density plasma that causes free radical damage to increases membrane permeability. Whereas at low repetition rates or with single femtosecond pulses, high density plasma is formed that produces thermoelastic stress leading to formation of cavitation bubbles which in turn cause cell permeabilization [16], [17].

3.4 APPLICATIONS

Optoporation has been applied to many different cell lines from CHO cells to stem cells for delivery of a wide variety of membrane impermeable materials, such as plasmid DNA [15], [18]–[25], exogenous dyes [15], [18], [21]–[25], macromolecules [26] and gold nanoparticles [27]. A number of studies have demonstrated different variations of optoporation with femtosecond lasers [19], [22], [28]–[33]. The ease of integration of optoporation setups with two photon microscopes is a major advantage. This has led to co-development with optical tweezer systems, where tightly focused laser beams are used to physically trap and insert a plasmid coated microparticle into a cell [32]. Studies for automating optoporation and increasing throughput have included integration with microfluidic channels or spatial light modulators. These can either change laser beam profile to target large cell populations or cell specific regions [19], [28]. Another approach to improve transfection efficiencies include optoporation of cells cultivated on graphene substrate [30] or addition of gold nanoparticles to the bath solution that attach unspecifically to cell membrane(GNOME technique) [34]–[36].

3.5 CHALLENGES AND APPLICATIONS FOR *In Vivo* SINGLE CELL OPTOPORATION

Most of the studies in the field of optoporation utilize high repetition rate systems and are applied to *in vitro* systems. As discussed in the previous chapter, these high repletion rate systems have low pulse energies and high average power which is

slightly above the powers used for nonlinear imaging. When applied to *in vivo* systems these suffer from both depth related scattering losses and insufficient energy to drive nonlinear absorption in the focal volume. Increasing the energy will lead to accumulation of thermal energy and damage the tissue at the focal volume [37]. This is a major challenge for the future of in vivo optoporation. This can be addressed by using low repetition rate 1 kHz regenerative amplifier systems. With peak intensities of 10^{13} W/cm^2 at the focal volume, it is capable of driving nonlinear multiphoton ionization and avalanche ionization generating a high density plasma that produce thermoelastic stresses and in turn lead to formation of transient cavitation bubbles that lead to dissection of cell membrane [16], [17], [38]. Previous studies have utilized this ablative mechanism to ablate blood vessels in mice cortex and model other neurological disease[39]–[41]. However, it has found little application for manipulation of a single cell deep inside a mouse cortex. Expanding this technique for transfection of a single cell is further discussed in Chapter 5. This work will open the doors to study development and diseases in a single cell in a live animal with high sterility, minimal invasiveness and high specificity. For example, this will allow us to study real time *in vivo* cell-cell interactions, early stages of tumor growth and arrest, functional connectivity of cortical neuronal circuits and other genetically-driven diseases.

3.6 CONCLUSION

With advancements in the field of laser based transfection, the stage is set for *in vivo* single cell optoporation. Expanding on previous studies, in the next chapter we

further establish the biophysical parameters for optoporation using a 1 kHz based amplifier system. Here we analyze the role of calcium in optoporation and cell viability. We quantify poration dynamics under the influence of different concentrations of calcium and further verify them using a fluorescence based calcium indicator. We further assess the hole resealing time and pore radius using inflow and outflow experiments with calcein AM and different sized fluorescently labeled dextran molecules respectively for a laser mediated membrane pore. Furthermore, in *vivo* studies involve cell targeting at depths up to 200um in the brain using both astrocyte labeling using sulforhodamine 101 and shadow patching with 150kDa FITC dextran. Thus, in this thesis, we establish a novel opotopration technique to enable single cell genetic manipulation in a live animal over a period of days and push forward biomedical research in this field.

REFERENCES

[1] T. K. Kim and J. H. Eberwine, “Mammalian cell transfection: the present and the future.,” *Anal. Bioanal. Chem.*, vol. 397, no. 8, pp. 3173–8, Aug. 2010.

[2] M. Wu *et al.*, “High-density distributed electrode network, a multi-functional electroporation method for delivery of molecules of different sizes.,” *Sci. Rep.*, vol. 3, p. 3370, Jan. 2013.

[3] P. E. Boukany *et al.*, “Nanochannel electroporation delivers precise amounts of biomolecules into living cells.,” *Nat. Nanotechnol.*, vol. 6, no. 11, pp. 747–54, Nov. 2011.

[4] S. K. Frandsen, H. Gissel, P. Hojman, T. Tramm, J. Eriksen, and J. Gehl, “Direct therapeutic applications of calcium electroporation to effectively induce tumor necrosis.,” *Cancer Res.*, vol. 72, no. 6, pp. 1336–41, Mar. 2012.

[5] K. Kitamura, B. Judkewitz, M. Kano, W. Denk, and M. Häusser, “Targeted patch-clamp recordings and single-cell electroporation of unlabeled neurons in vivo.,” *Nat. Methods*, vol. 5, no. 1, pp. 61–7, Jan. 2008.

[6] E. Neumann, M. Schaefer-Ridder, Y. Wang, and P. H. Hofschneider, “Gene transfer into mouse lyoma cells by electroporation in high electric fields.,” *EMBO J*, vol. 1, no. 7, pp. 841–845, 1982.

[7] K. Haas, W.-C. Sin, A. Javaherian, Z. Li, and H. T. Cline, “Single-Cell Electroporationfor Gene Transfer In Vivo,” *Neuron*, vol. 29, no. 3, pp. 583–591, Mar. 2001.

[8] J. C. Weaver and Y. A. Chizmadzhev, “Theory of electroporation: A review,” *Bioelectrochemistry Bioenerg.*, vol. 41, no. 2, pp. 135–160, Dec. 1996.

[9] H. R. Guzmán, D. X. Nguyen, S. Khan, and M. R. Prausnitz, “Ultrasound-mediated disruption of cell membranes. I. Quantification of molecular uptake and cell viability.,” *J. Acoust. Soc. Am.*, vol. 110, no. 1, pp. 588–96, Jul. 2001.

[10] I. Lentacker, I. De Cock, R. Deckers, S. C. De Smedt, and C. T. W. Moonen, “Understanding ultrasound induced sonoporation: definitions and underlying mechanisms.,” *Adv. Drug Deliv. Rev.*, vol. 72, pp. 49–64, Jun. 2014.

[11] L. Zhang, Y. & Yu, “Single-cell microinjection technology in cell biology,” *BioEssays*, vol. 30, p. 606–610., 2008.

[12] D. Gomez-Nicola, K. Riecken, B. Fehse, and V. H. Perry, “In-vivo RGB marking and multicolour single-cell tracking in the adult brain.,” *Sci. Rep.*, vol. 4, p. 7520, Jan. 2014.

[13] T. K. Kim and J. H. Eberwine, “Mammalian cell transfection: the present and the future.,” *Anal. Bioanal. Chem.*, vol. 397, no. 8, pp. 3173–8, Aug. 2010.

[14] M. Tsukakoshi, S. Kurata, Y. Nomiya, Y. Ikawa, and T. Kasuya, “A novel method of DNA transfection by laser microbeam cell surgery,” *Applied Physics B Photophysics and Laser Chemistry*, vol. 35. pp. 135–140, 1984.

[15] U. K. Tirlapur and K. König, “Targeted transfection by femtosecond laser.,” *Nature*, vol. 418, no. 6895, pp. 290–1, Jul. 2002.

[16] A. Vogel, J. Noack, G. Hüttman, and G. Paltauf, “Mechanisms of femtosecond laser nanosurgery of cells and tissues,” *Appl. Phys. B*, vol. 81, no. 8, pp. 1015–1047, Nov. 2005.

[17] A. V. and V. Venugopalan, “Mechanisms of Pulsed Laser Ablation of Biological Tissues,” *Chem. Rev.*, pp. 577–644, 2003.

[18] D. J. Stevenson, F. J. Gunn-Moore, P. Campbell, and K. Dholakia, “Single cell optical transfection.,” *J. R. Soc. Interface*, vol. 7, no. 47, pp. 863–71, Jun. 2010.

[19] R. F. Marchington, Y. Arita, X. Tsampoula, F. J. Gunn-Moore, and K. Dholakia, “Optical injection of mammalian cells using a microfluidic platform.,” *Biomed. Opt. Express*, vol. 1, no. 2, pp. 527–536, Jan. 2010.

[20] A. P. Rudhall *et al.*, “Exploring the ultrashort pulse laser parameter space for membrane permeabilisation in mammalian cells.,” *Sci. Rep.*, vol. 2, p. 858, Jan. 2012.

[21] J. Baumgart *et al.*, “Repetition rate dependency of reactive oxygen species formation during femtosecond laser-based cell surgery.,” *J. Biomed. Opt.*, vol. 14, no. 5, p. 54040, Jan. 2009.

[22] A. Uchugonova, K. König, R. Bueckle, A. Isemann, and G. Tempea, “Targeted transfection of stem cells with sub-20 femtosecond laser pulses.,” *Opt. Express*, vol. 16, no. 13, pp. 9357–64, Jun. 2008.

[23] F. Stracke, I. Rieman, and K. König, “Optical nanoinjection of macromolecules into vital cells,” *J. Photochem. Photobiol. B Biol.*, vol. 81, no. 3, pp. 136–142, 2005.

[24] C. T. A. Brown *et al.*, “Enhanced operation of femtosecond lasers and applications in cell transfection,” *J. Biophotonics*, vol. 1, no. 3, pp. 183–199, Aug. 2008.

[25] M. Lei, H. Xu, H. Yang, and B. Yao, “Femtosecond laser-assisted microinjection into living neurons,” *J. Neurosci. Methods*, vol. 174, no. 2, pp. 215–218, 2008.

[26] D. Heinemann *et al.*, “Delivery of proteins to mammalian cells via gold nanoparticle mediated laser transfection.,” *Nanotechnology*, vol. 25, no. 24, p. 245101, Jun. 2014.

[27] C. McDougall, D. J. Stevenson, C. T. A. Brown, F. Gunn-Moore, and K. Dholakia, “Targeted optical injection of gold nanoparticles into single mammalian cells,” *J. Biophotonics*, vol. 2, no. 12, pp. 736–743, 2009.

[28] M. Antkowiak, M. L. Torres-Mapa, F. Gunn-Moore, and K. Dholakia, “Application of dynamic diffractive optics for enhanced femtosecond laser based cell transfection.,” *J. Biophotonics*, vol. 3, no. 10–11, pp. 696–705, Oct. 2010.

[29] B. B. Praveen, D. J. Stevenson, M. Antkowiak, K. Dholakia, and F. J. Gunn-Moore, “Enhancement and optimization of plasmid expression in femtosecond optical transfection.,” *J. Biophotonics*, vol. 4, no. 4, pp. 229–35, Apr. 2011.

[30] P. Mthunzi, K. He, S. Ngcobo, T. Khanyile, and J. H. Warner, “Graphene for improved femtosecond laser based pluripotent stem cell transfection.,” *J. Biophotonics*, vol. 7, no. 5, pp. 351–62, May 2014.

[31] D. J. Stevenson, F. J. Gunn-Moore, P. Campbell, and K. Dholakia, “Single cell optical transfection.,” *J. R. Soc. Interface*, vol. 7, no. 47, pp. 863–71, Jun. 2010.

[32] Y. Arita, M. Ploschner, M. Antkowiak, F. Gunn-Moore, and K. Dholakia, “Single cell transfection by laser-induced breakdown of an optically trapped gold nanoparticle,” in *SPIE LASE*, 2014, p. 897203.

[33] P. Mthunzi, K. Dholakia, and F. Gunn-Moore, “Phototransfection of mammalian cells using femtosecond laser pulses: optimization and applicability to stem cell differentiation.,” *J. Biomed. Opt.*, vol. 15, no. 4, p. 41507, 2012.

[34] M. Schomaker *et al.*, “Biophysical effects in off-resonant gold nanoparticle mediated (GNOME) laser transfection of cell lines, primary- and stem cells using fs laser pulses.,” *J. Biophotonics*, vol. 8, no. 8, pp. 646–58, Aug. 2015.

[35] D. Begandt *et al.*, “Gold nanoparticle-mediated (GNOME) laser perforation: a new method for a high-throughput analysis of gap junction intercellular coupling.,” *J. Bioenerg. Biomembr.*, Aug. 2015.

[36] J. Baumgart, L. Humbert, É. Boulais, R. Lachaine, J.-J. Lebrun, and M. Meunier, “Off-resonance plasmonic enhanced femtosecond laser optoporation and transfection of cancer cells.,” *Biomaterials*, vol. 33, no. 7, pp. 2345–50, Mar. 2012.

[37] A. A. Davis, M. J. Farrar, N. Nishimura, M. M. Jin, and C. B. Schaffer, “Optoporation and genetic manipulation of cells using femtosecond laser pulses.,” *Biophys. J.*, vol. 105, no. 4, pp. 862–71, Aug. 2013.

[38] C. Schaffer, N. Nishimura, E. Glezer, A. Kim, and E. Mazur, “Dynamics of femtosecond laser-induced breakdown in water from femtoseconds to microseconds,” *Opt. Express*, vol. 10, no. 3, p. 196, Feb. 2002.

[39] C. Schaffer, N. Nishimura, E. Glezer, A. Kim, and E. Mazur, “Dynamics of femtosecond laser-induced breakdown in water from femtoseconds to microseconds,” *Opt. Express*, vol. 10, no. 3, p. 196, Feb. 2002.

[40] N. L. Rosidi *et al.*, “Cortical microhemorrhages cause local inflammation but do not trigger widespread dendrite degeneration.,” *PLoS One*, vol. 6, no. 10, p. e26612, Jan. 2011.

[41] N. Nishimura, C. B. Schaffer, B. Friedman, P. S. Tsai, P. D. Lyden, and D. Kleinfeld, “Targeted insult to subsurface cortical blood vessels using ultrashort laser pulses: three models of stroke.,” *Nat. Methods*, vol. 3, no. 2, pp. 99–108, Feb. 2006.

[42] “Transfection Methods,” *Life Technologies*. [Online]. Available: http://www.ugent.be/inedc.html%0A.

CHAPTER 4

BIOPHYSICAL CHARACTERIZATION OF IN VITRO OPTOPORATION

This chapter is the manuscript for a future paper. That will be tentatively titled as follows

Gadamsetty, P., Kalies, S., Patis, L., and Schaffer, CB., Influence of calcium on membrane optoporation and resealing dynamics in 1 kHz femtosecond laser regime, 2017

4.1 ABSTRACT

Optoporation allows the minimally invasive transfer of extracellular molecules into cells. The use of a low repetition rate laser system (100 fs at 790 nm and 1kHz repetition rate) can enable the future transfer of this technique to *in vivo* applications. However, it is essential to understand the biophysical parameter space of this technique beforehand. Based on our previous study, we examined the optoporation dependence on the extracellular calcium concentration in HeLa cells. We observed a low cell recovery rate in calcium free medium and varying cell viabilities with different calcium concentrations, pointing toward calcium dependent repair processes. The resealing time exhibited a trend to decrease with increasing calcium concentrations. Also we followed the calcium rise in the cell by a fluorescent calcium indicator. It was delayed in calcium free medium and the rise was significantly increased with the highest applied extracellular calcium concentration. Furthermore, we extended our previous model of pore formation model and applied different sized dextrans to verify our assumptions on pore radius, and resealing time. Therefore, this study provides a better understanding of the biophysical processes accompanying single cell laser transfection.

4.2 INTRODUCTION

The cell membrane of a mammalian cell is impermeable to macromolecules like nucleic acids or most proteins. The process of introducing these exogenous molecules

into cells is generally termed cell transfection and today accomplished by a variety of techniques including chemical, biological or physical methods[1].

A well-established example of transfection is liposomal transfection which utilizes complexes of nucleic acids and liposomes to overcome the cell membrane barrier in an endocytosis mediated process. However, it is not generally applicable to all cell lines with the same efficiency and cannot be targeted to specific cells in a mixed cell population. Electroporation is another cell transfection technique based on electrical pulses which induce a dipole moment in the cell membrane, which leads to the formation of hydrophilic pores on the membrane[2], [3]. This technique is highly efficient and can also be applied on a single cell level today[4].

In 1984, the first demonstration of laser based transfection by Tsukakoshi et al. was accomplished[5]. It has the advantage of single cell spatial selectivity. Tirlapur et al. introduced the application of femtosecond laser pulses for cell transfection and obtained high transfection efficiencies using this method[6]. The femtosecond pulses are focused with a high numerical aperture objective on the cell membrane. As the pulse length is significantly shorter than the thermal diffusion time in water no extensive heating occurs next to the manipulation spot[7], [8]. Instead, multiphoton ionization of water leads to the formation of seed electrons which are accelerated by inverse bremsstrahlung of the laser irradiation[8]. Depending on the applied intensity this can either evoke the formation of a low density plasma , in which chemical modification of biomolecules can occur, or induce the formation of optical breakdown[8], [9].

Additionally, cavitation bubble formation occurs with high electron densities[9]. Usually, processes below the optical breakdown are used for permeabilization of the cell membrane and have been recently investigated in detail by Rudhall et al[10].

Several different settings and modifications have been employed in femtosecond laser transfection[7], [11]–[16]. For example, it was shown to be applicable in stem cells with a change in efficiency depending on the applied pulse length or the passage number of the cells[11], [12]. Additionally, cultivation of the cells on a graphene substrate might improve transfection efficiencies[16]. Further modifications include the use of a microfluidic channel setup to reach higher numbers of transfected cells on the same time scale, or the application of a spatial light modulator to change the manipulation laser beam profile or to target specific cell regions[13], [14]. Another approach utilizes gold nanoparticles which are attached unspecific ally to the cell membrane to enable high-throughput laser transfection[17], [18].

Most of the femtosecond laser transfection studies utilized high repetition rate laser and low pulse energy systems. These operate slightly above the power for nonlinear imaging. For *in vivo* applications, these low laser energies will suffer from scattering losses and have insufficient energy for nonlinear absorption to occur in the focal volume. Thermal energy will also accumulate as the heat cannot dissipate from the focal volume[19]. This is a major drawback for future *in vivo* applications. To address this issue, high pulse energies are needed. We demonstrated femtosecond based laser transfection with a low rep rate 1Khz regenerative amplifier and 2-3 pulses at high

pulse energies of 11-14nJ. This results in the formation of a high density plasma though avalanche and multiphoton ionization at the focussing volume. At 1 NA focussing and being above the threshold for breakdown of water, plasma membrane pore forms by ablative damage and vaporization of the material. This ablative mechanism has been used to ablate blood vessels in mice cortex to model diseases[9,20,21]. A comparison to an oscillator based system at 80 MHz yielded comparable transfection efficiencies of around 45%. Additionally, the outflow of Calcein AM in regular cell media for both amplifier and oscillator laser system was analyzed in this study and a diffusion model was applied to obtain the pore releasing time and its initial radius[19].

In this study, we extend this investigation to the biophysical changes of the cell membrane during optoporation. To the best of our knowledge, the biophysical changes in the cell have currently only been investigated for gold nanoparticle mediated laser transfection but not for single cell transfection[22]. We analyze the poration efficiency and cell viability in different extracellular calcium solutions, because calcium is a key mediator of membrane repair and resealing. Based on our previous model for pore formation we quantify the initial radius and resealing times of the pore for these concentrations and relate it to the calcium influx examined by a fluorescence based calcium indicator. To further elucidate the pore formation and for further validation of our model, we investigate the inflow of different sized fluorescently labeled dextran molecules.

4.3 METHODS

4.3.1 Cell culture

These experiments used adherent HeLa cells for opotoporation. The HeLa cells were incubated in a 5% CO_2/95% air incubator at 37^0C. Cells were grown in T-25 flask (Corning, Corning, NY) and plated in 35mm glass-bottomed culture dishes (MatTek, Ashland, MA) to form a single sub-confluent layer. The growth medium for cell growth consisted of Advanced DMEM (Life Technologies, Grand Island, NY), 10% FBS (Life Technologies, Grand Island, NY), 1% penicillin/streptomycin (Life Technologies, Grand Island, NY) and 1% GlutaMAX solution (Life Technologies, Grand Island, NY). During the optoporation experiments with Calcein AM, calcium and dextran solutions, DMEM/F-12 (Life Technologies, Grand Island, NY) without phenol red was used to replace regular cell culture medium.

4.3.2 Two-photon excitation fluorescence microscopy

Imaging was done using a custom built four detection channel two-photon microscope. A Ti:Sapphire laser system laser (MIRA-HP; Coherent, Santa Clara, CA) with 100 fs pulse duration, 800 nm central wavelength, 10 nm FWHM bandwidth, and 76 MHz repetition was used. All imaging experiments used a Zeiss 20x magnification 1.0 NA upright microscope objective with water immersion (Zeiss, Thornwood, NY). Fluorescence collection was achieved using a 530-nm bandpass filter with 41-nm

bandwidth. ScanImage (r3.8.1, Janelia Farm, USA) was used for image acquisition. Time lapse image acquisition for Calcein AM and dextran experiments was set at 3.15 frames/sec and 512x512 pixels, and calcium experiments were at 7.51 frames/sec at 256x256 pixels. Image analysis and processing used custom written scripts in MATLAB (The MathWorks, Natick, MA) and ImageJ.

4.3.3 Regenerative amplifier for membrane ablation

A high pulse energy and low repetition rate regenerative Ti:Sapphire amplifier (Legend-USP; Coherent, Santa Clara, CA) was used for targeted optoporation of the cell membrane. It operated at 100 fs pulse duration, 790 nm central wavelength, 25nm FWHM bandwidth, and 1 kHz repetition rate. Neutral density filters, a fast mechanical shutter, a function generator, and an oscilloscope were applied to monitor and control the incident energy and number of pulses at each targeted site on the cell. One to three pulses were applied on the membrane target site. A polarizing beam splitter cube allowed to combine imaging and manipulation beam in the microscope setup and focussing the ablation beam in the centre of the imaging plane. The pulse energy at the objective was determined to be in the range of 11- 14nJ.

4.3.4 Cell labelling with Calcein AM and Oregon Green BAPTA

HeLa cells for outflow experiments were labelled with Calcein-AM (Life Technologies, Grand Island, NY) at a concentration of 800 nM and incubated for 20

min at 37^0C. To assess the calcium response after optoporation, cells were loaded with Oregon Green 488 BAPTA-1 calcium indicator (Life Technologies, Grand Island, NY). After the addition of 2.25 μM indicator dye the cells were incubated for 20-30 mins at 37C.

In the case of Calcein AM and oregon green BAPTA, each dish was washed two times to remove any trace of the dye before being replaced with supplement-free and phenol red-free DMEM for imaging. This step was necessary to avoid any background fluorescence.

The influence of calcium on the optoporation and resealing process was observed in different calcium concentrations which were realized by the addition of $CaCl_2$ (Sigma Aldrich, St. Louis, MO) to calcium free DMEM. The pH of the media was adjusted to 7.2. Each media change was preceded by at least two washing steps of the cells and the microscope objective with the medium applied in the subsequent experiment.

4.3.5 Model and kinetics of pore radius and resealing time

We used the outflow of Calcein from an optoporated cell to determine the pore resealing time and its initial radius (see section 3.1). Compared to our previous study we included a correction for the pore radius for large pores. It takes into account the small length of the membrane compared to the large pore size. Because no stirring occurs in far distance from the pore, we cannot assume a uniform concentration at these

sites. The total change of concentration $d\Phi(t)/dt$through the pore changes compared to our previous study to[23]:

$$\frac{d\Phi(t)}{dt} = -\frac{\pi r^2 D}{(e + \frac{2\pi r}{4})V}\,\Phi(t)$$

with an effective thickness of: $e' = \mathrm{e} + \pi r/2$. In the formula D is the diffusion coefficient of Calcein in water which is 3.63e-10 m^2s^{-1}, e is the membrane thickness of 10 nm, and V is the cell volume (approx. 1200 μm^3). The pore radius is r and to be determined by the model. It is interesting to note that in the limit of large pores, the concentration change reduces to:

$$\frac{d\Phi(t)}{dt} = \frac{-2\mathrm{r}D\Phi(t)}{V}$$

Based on our previous model, we fitted the fluorescence decrease with an exponential function of the form: $\Phi(t) = \Phi(0)\exp\left(-\frac{t}{\tau}\right)$ with:

$$\tau = \frac{(e + \frac{2\pi r}{4})V}{\pi r^2 D}$$

and numerically derived the initial pore radius from this fit. The resealing time is given by:

$$t_{hole} = log(\frac{\Phi(0)}{\Phi(\infty)})$$

4.3.6 Inflow of different sized dextrans

To further elucidate the biophysical mechanisms of optoporation, we applied four different sized, fluorescently labelled dextrans: 10 kDa, 150 kDa, 500 kDa and 2 MDa (Sigma Aldrich, St. Loius, MO). A fixed concentration of 0.2 mg/ml was added to the cells in regular cell culture medium. Between each imaging session the objective was rinsed twice to remove any trace of previous dye before the next cell culture dish was imaged. Cells were black objects in the fluorescent dextran solution and the inflow of dextrans was examined by manually outlining the cell and the perforation spot in ImageJ software. For the small sized dextrans of 10 kDa, we applied our model with a diffusion coefficient of 1.3e-10 $m^{-2}s$ and for 150 kDa dextran we used diffusion coefficient of 2.3e-11 $m^{-2}s$ [25,26] .

4.3.7 Statistics

Statistical comparisons were performed as multi parameter correction for t-test (divide p criteria by 2) indicated in the respective results section. Tests included Student's t-test and Cuzick's test for trend. Results were considered significant when $p < 0.05$. All boxplots display the 25th to 75th percentile (box), the median (red line), and the mean (blue cross). Whiskers represent the data within 1.5 times the interquartile range from the 25th to 75th percentile. Points that fell outside the range of the whiskers were identified as outliers and excluded by a red cross through the data point and in the calculation of the mean value.

4.4 RESULTS

4.4.1 Influence of Ca^{2+} concentration on cell viability during perforation

We analysed the outflow of Calcein AM to determine if a cell was successfully perforated, unchanged or killed by the perforation procedure. Perforated, living cells showed a Calcein AM outflow which remained constant at around half its initial value after a certain resealing time of around 90 s (see Figure 1a and b), while dead cells exhibited an ongoing outflow connected to a large decrease in cell fluorescence. The fluorescence of unchanged cells remained same.

Based on these criteria, we derived the number of perforated, dead or unchanged cells with different calcium concentrations with about 80-130 cells targeted in each group (see Figure 1c). In cell media without calcium most cells died. The total number of dead cells was about 60% in this group. This value is similar to the value observed with 10 mM extracellular calcium. The highest number of perforated, viable cells was obtained in medium with 1 mM Ca^{2+}. In 3, 5 and 10 mM Ca^{2+} supplemented medium the highest number of unchanged cells was observed. It equalled the number of perforated cells in 3 mM Ca^{2+}.

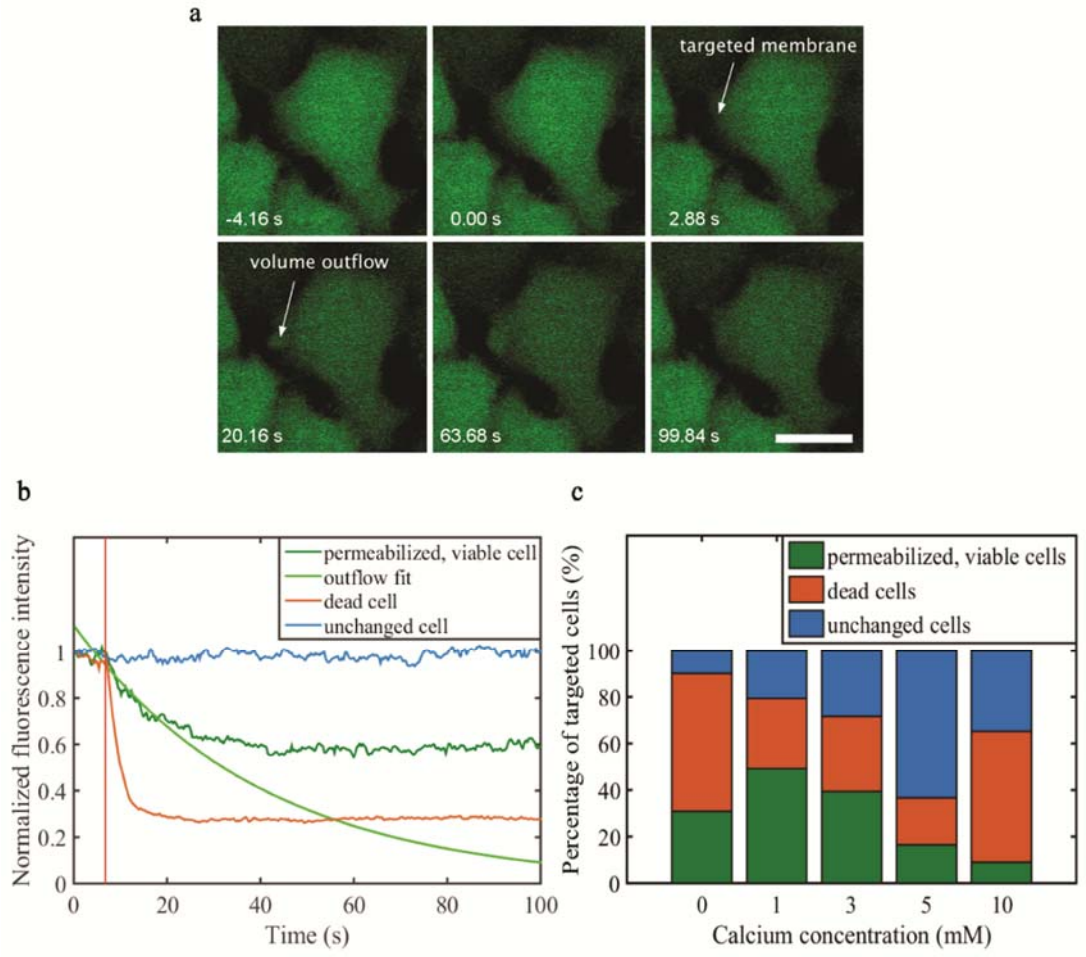

Figure 1 Influence of calcium concentration on the the cell viability after optoporation. a) Exemplary fluorescence images of a successfully optoporated cell, showing the outflow of dye at the poration site. Scale bar 20 um. b) Exemplary fluorescence decrease for a permeabilized, viable cell compared to an unchanged or dead cell over time and corresponding fit function for optoporation model. c) Percentage of observed change for all cells for the different calcium concentrations. With 1 mM extracellular calcium most cells were successfully optoporated. An extracellular calcium concentration of 0 mM and 10 mM led to elevated levels of dead cells.

4.4.2 Dependence of pore radius and pore resealing time on Ca^{2+} concentration

Based on the model described in the methods section we determined the pore resealing time and initial cell radius of perforated, viable cells and analysed their dependence on the extracellular Ca2+ concentration (see Figure 1b).

The initial pore radius ranged between a few and hundred nanometres with a median around 35 nm in all different applied media, except for calcium free medium with 20 nm (see Figure 2b). No significant trend and dependence on the Ca2+ concentration was observed for the radius ($p=0.087$, 1-sided Cuzick's test for non-parametric trend analysis). The pore resealing time was strongly elevated for 0 mM Ca2+ compared to all other applied concentrations (see Figure 2b). We observed a significant trend for increasing calcium concentrations for the resealing time ($p<0.0004$, 1-sided Cuzick's test).

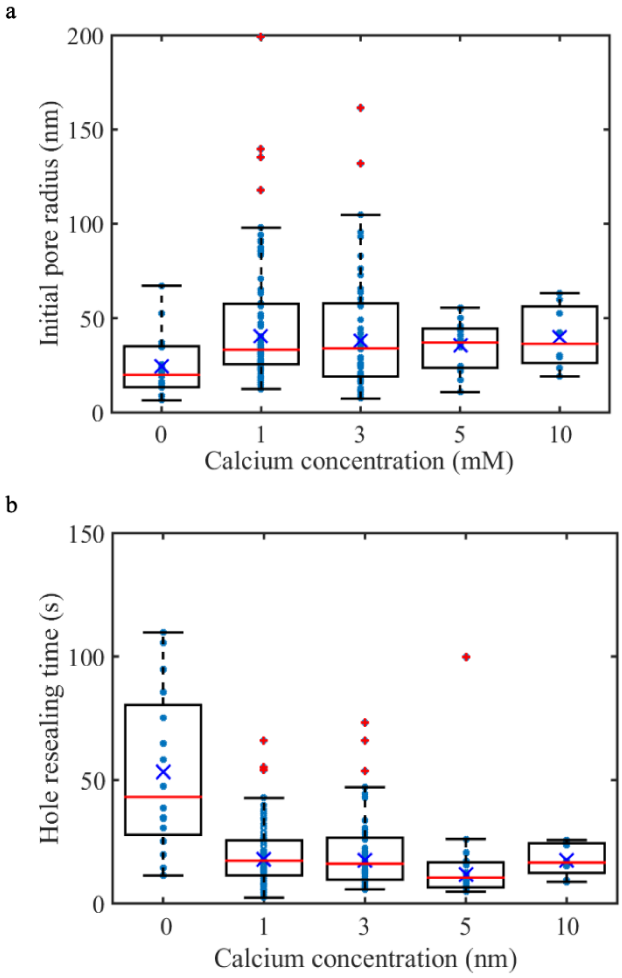

Figure 2 Initial pore radius (a) and hole resealing time (b) for different concentrations of extracellular calcium. The initial radius varied around 40 nm and did not exhibit a significant trend for the different calcium concentrations. The hole resealing time showed a trend with increasing calcium concentration. It was highest in medium without any extracellular calcium.

4.4.3 Calcium kinetics after cell perforation

We examined the calcium rise within the cell with the calcium indicator Oregon Green BAPTA. Upon inflow or intracellular release of calcium due to membrane optoporation, the dye fluorescence increased (see Figure 3 a). We characterized the time required for this rise, the fluorescence difference to the initial cell fluorescence, and the duration of the calcium plateau. The rise is fast compared to? the resealing time and consequently unaffected by dye outflow. The plateau time is influenced by the onset of photobleaching, dye outflow through perforation, and by cell mechanisms of calcium pumping and can only serve as a weak indicator compared to the duration of the calcium rise and the difference in fluorescence.

The duration of the calcium rise was significantly longer in cells in calcium free medium compared to medium with 1 mM or 10 mM calcium (see Figure 3b, $p<0.008$, 2-sided Student's t-test). Between the latter groups no significant difference was observed ($p=0.48$, 2-sided Student's t-test).

The fluorescence difference compared to the initial fluorescence of the calcium indicator dye was significantly higher in medium supplemented with 10 mM calcium (see Figure 3c, $p<1.4e-5$). The duration of the plateau was 3 s in this case and also significantly longer than for 0 mM and 1 mM ($p<3.0e-4$). Between 0 mM and 1 mM the fluorescence increase did not differ significantly ($p=0.81$) and the plateau time was similar ($p=0.13$).

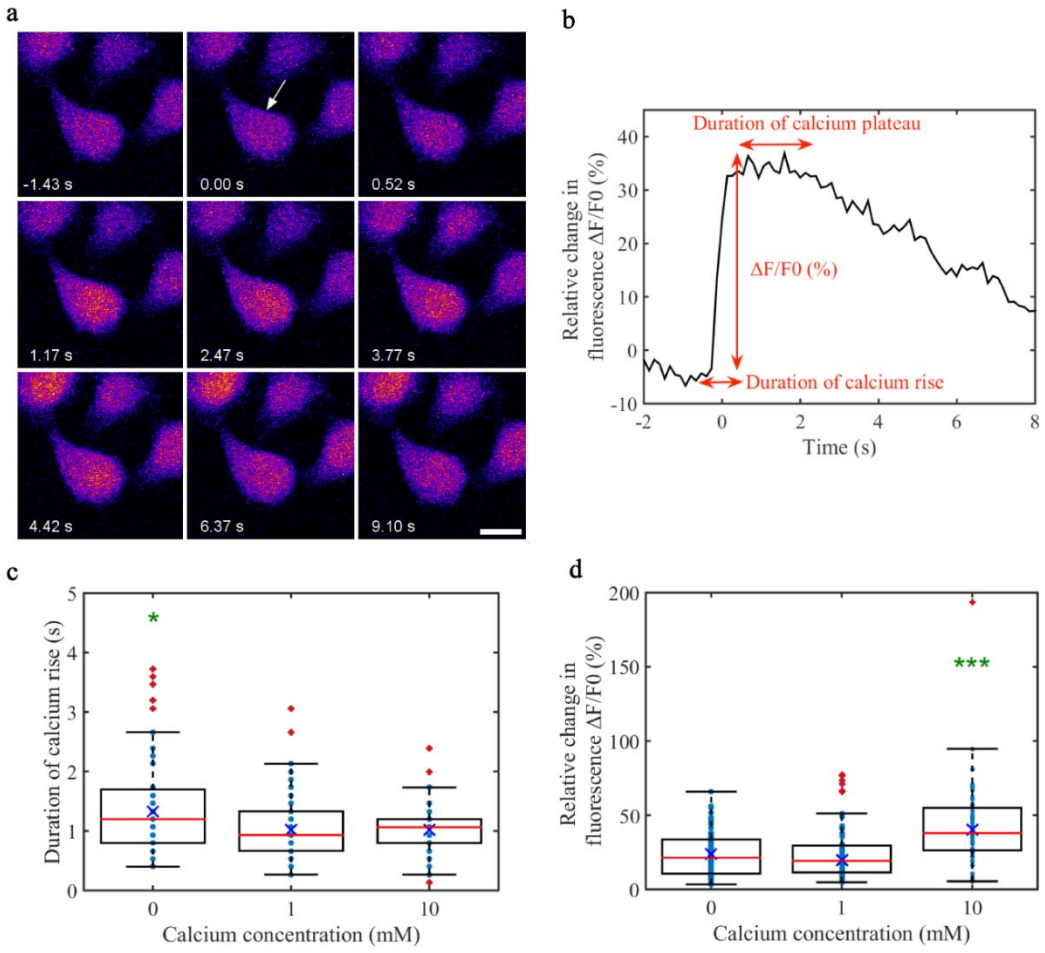

Figure 3 Influence of calcium concentration on the calcium response of the cell after optoporation. Scale bar 20 um. a) Fluorescent images of optoporated cells stained with calcium indicator dye Bapta Oregon Green. b) Exemplary curve for an extracellular calcium concentration of 1 mM. c) Dependence of the duration of the calcium rise on the extracellular calcium concentration. The rise is significantly longer in calcium free extracellular medium. d) The relative change in calcium fluorescence based on the initial cell fluorescence for 0, 1 and 10 mM calcium is significantly elevated for 10 mM extracellular calcium.

4.4.4 Analysis of inflow of different sized dextrans for pore size and resealing time validation

Four different dextran sizes were applied and the inflow kinetics were recorded based on the fluorescence increase within the optoporated cell compared to the surrounding. All four dextran sizes could be delivered into the cell with the optoporation system (see Figure 4 a,b,c,d). While we observed an increase of the fluorescence of the whole cell for 10 kDa and 150 kDa dextrans in successfully optoporated cells, the signal for 500 kDa and 2 MDa dextrans was usually limited to the spot of membrane optoporation. Therefore, the delivery efficiency of 10 and 150 kDa dextrans was much higher than for the higher dextran sizes.

This can be explained by looking at the calculated number of dextrans for a fixed radius of 50 nm (see Figure 4 b). Here, we observe that maximum inflow of about 10^6 molecules occur for 10 kDa dextrans and minimum of 400-500 molecules for 2 MDa dextrans. In addition, our previous studies have shown that in the case of plasmid DNAs, about 10 plasmids enter in the cytosol upon optoporation.Based on these observations, we decided to analyse the fluorescence increase in the area around the optoporation site and of the whole cell after optoporation (see Figure 4 a). For all dextrans, we typically observed a short peak in fluorescence at the optoporation site of about 20 s in viable cells (see Figure 4 a, c). This peak width indicates a similar hole resealing time for all different sized dextrans.

The cell fluorescence was not reliably evaluable for 500 kDa and 2000 kDa as photobleaching and slow diffusion from the perforation spot in three dimensions influenced the signal. In the case of 10 kDa and 150 kDa dextrans, we analysed the fluorescence of the whole cell. We applied the same model as for the Calcein outflow and treated the extracellular maximum fluorescence as background (inverse image stack). We observed similar hole resealing times to Calcein outflow in this case. The initial pore radius was larger for 10 kDa dextrans, and especially larger for 150 kDa dextrans. We used diffusion coefficients of 1.3e-10 m-2s and 2.3e-11 m-2s for 10 kDa and 150 kDa dextrans, respectively (Du et al. 2010; Schnell et al.) . The increase in the initial radius could be based on the used diffusion coefficients or hinderence of FITC dextran diffusion due to the larger size of the dextrans compared to Calcein.

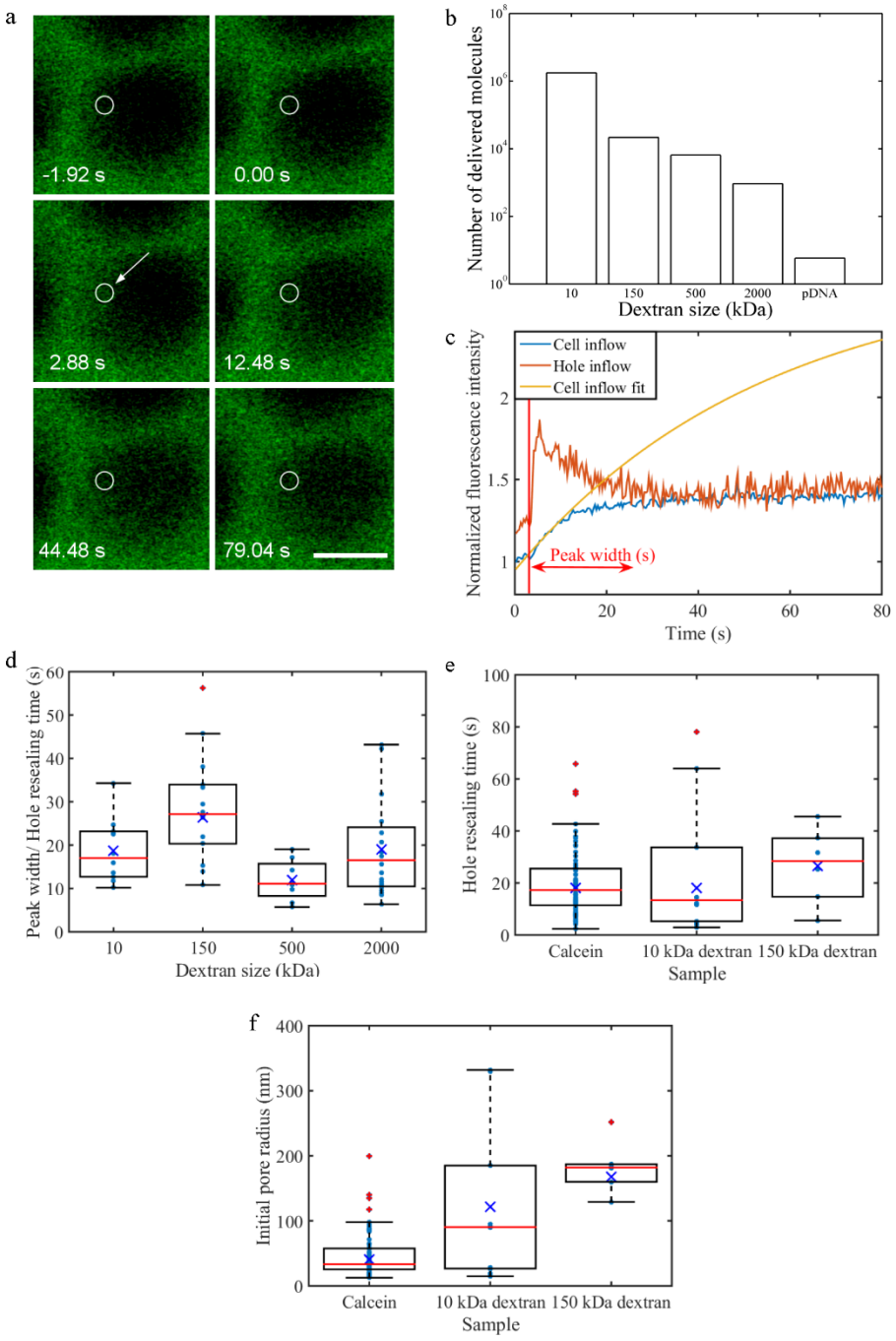

Figure 4 Inflow of different sized, fluorescently labeled dextrans into the cell for a fixed extracellular calcium concentration of 1 mM. a) Exemplary fluorescence images for 10 kDa dextran. b) Calculated number of dextran molecules which would enter the cell for a fixed radius of 50 nm. c) Exemplary graph of a), the inflow and gain of fluorescence was analyed in the whole cell and at the spot of perforation. In viable cells, a peak of about 20 s was observed at the optoporation spot (c) which did not show a significant trend for increasing dextran sizes (d). The total fluorescence of the cell was analyzed with the same model used for Calcein outflow and fitted appropriately for an inverse image stack. e) The hole resealing time obtained from the fit was similar for the 10 kDa and 150 kDa dextrans to the Calcein for 1 mM from Figure 2. f) The calculated pore radius depends on the diffusion coefficient and increased with the dextran size, possibly due to an accumulation of dextrans at the spot of optoporation or hindered diffusion due to the large molecule size within the cell.

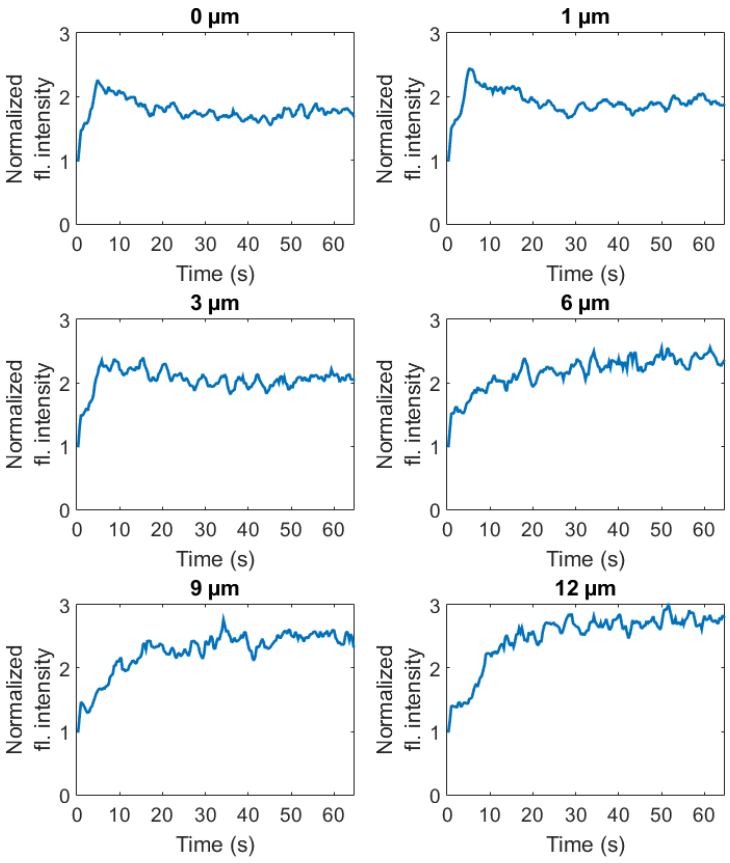

Figure 5 Influence of calcium on membrane optoporation and resealing dynamics in 1 kHz femtosecond laser regime Exemplary graphs of 10 kDa FITC dextran fluorescence intensity over time at various distances away from the perforation site inside the cell. Data was obtained for a line of 1x20px and smoothed with a 2 dimensional convolution filter of 6x6 size in Matlab.

4.5 DISCUSSION AND CONCLUSION

In this study, we extended our investigations on optoporation with a low repetition rate 1kHz laser system and analysed the dependence of the perforation kinetics on the extracellular calcium concentration. Additionally, the inflow of different sized dextrans was examined to support our pore model of diffusion.

Post disruption, nucleated cells are capable of staying viable by rapid membrane resealing [26]. This is crucial for successful membrane optoporation, in particular when ablation of the cell membrane in the high pulse energy regime is the underlying mechanism. Former studies with laser or mechanically induced membrane wounds have shown that nucleated cells reseal within seconds to minutes[24,25].

Resealing can occur through a single or multiple mechanisms: line tension induced spontaneous resealing, homotypic fusion with patch formation, exocytotic reduction, or endocytosis, where vesicles fuse to form a patch at the damaged site [26], [27]. Spontaneous resealing generally occurs for wounds <1µm in nucleated cells. Homotypic fusion has the resealing capacity for very large disruption. Calcium is one of the key mediators in successful membrane resealing. The literature is currently expanding to include several calcium dependant proteins that lead the resealing when intracellular Ca^{2+} rises post membrane disruption. Mechanisms of membrane resealing are driven by both, size of the damaged membrane site, and the intracellular and extracellular Ca^{2+}concentration. Resealing process have an essential requirement of a

critical rise in intracellular Ca^{2+}. If this threshold is crossed, resealing is initiated and if it exceeds a higher threshold by large influx of Ca^{2+}, it can be toxic to the cell and failure of the resealing mechanisms[28,29,30,31,27]. This explains the different findings for the cell viability and perforation efficiency in different calcium concentrations (see section 3.1). In particular, we observed that 10 mM and 0 mM extracellular calcium solution caused maximum cell death ~60%, which is in agreement with no or possibly toxic inflow. The significant elevated inflow of calcium was also observable using the calcium indicator dye Bapata Oregon Green. The majority of the cells in 3 mM, 5mM and 10mM extracellular solution remained unchanged, which could either indicate that the pore closed before we could quantify the change in fluorescence or no change happened.

Based on these initial observations, we used an extended pore formation model to address the kinetics of outflow and inflow from the optoporated cells, to quantify resealing time and pore radius. The resealing time was significantly elevated without extracellular calcium while we still observed a calcium response with the calcium indicator dye. This can be explained by a delayed intracellular rise in calcium, which is possibly mediated by processes like inositol triphosphate release at the damaged membrane, and was also observed in our experiments. Additionally, resealing time significantly decreases across 0 mM to 10 mM cases. It is likely that extracellular calcium aids the intracellular calcium in rising up to critical levels and expedite resealing. The lower calcium concentration provided intracellularly could explain the longer resealing time and lower cell viability without extracellular calcium. Compared

to this, Baumgart et al had demonstrated that optoporation in medium containing the calcium chelator EGTA inhibited rise in intracellular calcium with 160,000 pulses. The optoporation in this case possibly leads to inflow of EGTA which binds the intracellular released calcium, while in our case of 2-3 pulses, no chelation agent is used, which did not inhibit any intracellular calcium.

In contrast to the resealing time, we observed that the radii do not change significantly under different extracellular calcium concentrations, which agrees with the laser pulse energy being probably the only contributing factor for the ablation of a given part of the cell membrane.

The maximum perforation efficiency of ~45% at pulse energies of 11-15nJ was achieved at 1mM extracellular calcium, which represents normal cell medium. This energy and viability rate agrees well with our previously reported rate for optoporation with low repetition rate lasers. We extended our previous model of the pore formation by including variations of the flow way depending on the pore radius and membrane thickness.

To further investigate the kinetics, we examined the inflow of different sized dextrans into the cells. Interestingly we found uptake of dextrans of sizes up to 2000 kDa into the cell, similar to other laser transfection approaches employing gold nanoparticles. This represents a variety of biologically relevant molecules in size. In our former study we observed that pDNA enters the cell at the site of optoporation through

adherence on the damaged membrane and translocation into the cytoplasm about 30 min after otpororation. While pDNA has a weight in the range of a few thousand kDA, a significant difference to the 2000 kDa dextran would be that pDNA is negatively charged. This charge would hinder diffusion through a pore created by optoporation due to a gradient from the inner negatively charged to the outer positively charged outlet of the plasma membrane. However, the accumulation of pDNA at the outer leaflet of the membrane is very likely due to the charge difference.

Further observations showed that a short peak in fluorescence lasting between 15-30 s indicated successful delivery at the poration site for all dextran sizes. This peak is in well agreement with our resealing time derived by the poration model and indicates therefore closure of pores. For small dextrans of 10 kDa and 150 kDa which were delivered into the cell in significant amounts, these distribute in the cell in the following time.

We also employed our model for obtaining the resealing time based on 10 kDa and 150 kDa dextrans in viable cells. We obtained resealing times of 28 and 35 seconds respectively, which is in good agreement with the predictions by the model and Calcein outflow.

The initial pore radius estimates of 150 kDa particles are larger than that of 10 kDa particles. Taking into consideration our model's assumptions, this could either indicate accumulation of large particles at the pore that increases its relative size or hindrance

induced slower diffusion. Similarly, due to larger sizes of 500 kDa and 2 MDa, there was more hindrance and minimal inflow into the cell that the fluorescence change was not significant.

In conclusion, we have quantified the role of calcium in optoporation and have an extended model of membrane pore dynamics. In addition, we have further re-verified our model with inflow and size based experiments. Importantly, we have shown that these calcium based perforation kinetics are capable of fitting in our model and can be effectively used to further understand the role calcium plays in post optoporation based plasma membrane resealing. These findings particularly for laser regimes of 1 kHz repetition rates open the door to *in vivo* experiments and better understanding of the biophysical parameters that underlie it. Future studies, using the minimally invasive and high selectivity technique that optoporation provides will be critical for development of targeted genetic manipulation of single cells *in vivo* to further our understanding of diseases at cellular levels.

REFERENCES

[1] T. K. Kim and J. H. Eberwine, “Mammalian cell transfection: the present and the future.,” *Anal. Bioanal. Chem.*, vol. 397, no. 8, pp. 3173–8, Aug. 2010.

[2] E. Neumann, M. Schaefer-Ridder, Y. Wang, and P. H. Hofschneider, “Gene transfer into mouse lyoma cells by electroporation in high electric fields.,” *EMBO J*, vol. 1, no. 7, pp. 841–845, 1982.

[3] J. C. Weaver and Y. A. Chizmadzhev, “Theory of electroporation: A review,” *Bioelectrochemistry Bioenerg.*, vol. 41, no. 2, pp. 135–160, Dec. 1996.

[4] K. Haas, W.-C. Sin, A. Javaherian, Z. Li, and H. T. Cline, “Single-Cell Electroporationfor Gene Transfer In Vivo,” *Neuron*, vol. 29, no. 3, pp. 583–591, Mar. 2001.

[5] M. Tsukakoshi, S. Kurata, Y. Nomiya, Y. Ikawa, and T. Kasuya, “A novel method of DNA transfection by laser microbeam cell surgery,” *Applied Physics B Photophysics and Laser Chemistry*, vol. 35. pp. 135–140, 1984.

[6] U. K. Tirlapur and K. König, “Targeted transfection by femtosecond laser.,” *Nature*, vol. 418, no. 6895, pp. 290–1, Jul. 2002.

[7] D. J. Stevenson, F. J. Gunn-Moore, P. Campbell, and K. Dholakia, “Single cell optical transfection.,” *J. R. Soc. Interface*, vol. 7, no. 47, pp. 863–71, Jun. 2010.

[8] A. Vogel, J. Noack, G. Hüttman, and G. Paltauf, “Mechanisms of femtosecond laser nanosurgery of cells and tissues,” *Appl. Phys. B*, vol. 81, no. 8, pp. 1015–1047, Nov. 2005.

[9] C. Schaffer, N. Nishimura, E. Glezer, A. Kim, and E. Mazur, "Dynamics of femtosecond laser-induced breakdown in water from femtoseconds to microseconds," *Opt. Express*, vol. 10, no. 3, p. 196, Feb. 2002.

[10] A. P. Rudhall *et al.*, "Exploring the ultrashort pulse laser parameter space for membrane permeabilisation in mammalian cells.," *Sci. Rep.*, vol. 2, p. 858, Jan. 2012.

[11] P. Mthunzi, K. Dholakia, and F. Gunn-Moore, "Phototransfection of mammalian cells using femtosecond laser pulses: optimization and applicability to stem cell differentiation.," *J. Biomed. Opt.*, vol. 15, no. 4, p. 41507, 2012.

[12] A. Uchugonova, K. König, R. Bueckle, A. Isemann, and G. Tempea, "Targeted transfection of stem cells with sub-20 femtosecond laser pulses.," *Opt. Express*, vol. 16, no. 13, pp. 9357–64, Jun. 2008.

[13] R. F. Marchington, Y. Arita, X. Tsampoula, F. J. Gunn-Moore, and K. Dholakia, "Optical injection of mammalian cells using a microfluidic platform.," *Biomed. Opt. Express*, vol. 1, no. 2, pp. 527–536, Jan. 2010.

[14] M. Antkowiak, M. L. Torres-Mapa, F. Gunn-Moore, and K. Dholakia, "Application of dynamic diffractive optics for enhanced femtosecond laser based cell transfection.," *J. Biophotonics*, vol. 3, no. 10–11, pp. 696–705, Oct. 2010.

[15] B. B. Praveen, D. J. Stevenson, M. Antkowiak, K. Dholakia, and F. J. Gunn-Moore, "Enhancement and optimization of plasmid expression in femtosecond optical transfection.," *J. Biophotonics*, vol. 4, no. 4, pp. 229–35, Apr. 2011.

[16] P. Mthunzi, K. He, S. Ngcobo, T. Khanyile, and J. H. Warner, “Graphene for improved femtosecond laser based pluripotent stem cell transfection.,” *J. Biophotonics*, vol. 7, no. 5, pp. 351–62, May 2014.

[17] M. Schomaker *et al.*, “Characterization of nanoparticle mediated laser transfection by femtosecond laser pulses for applications in molecular medicine.,” *J. Nanobiotechnology*, vol. 13, no. 1, p. 10, Jan. 2015.

[18] J. Baumgart, L. Humbert, É. Boulais, R. Lachaine, J.-J. Lebrun, and M. Meunier, “Off-resonance plasmonic enhanced femtosecond laser optoporation and transfection of cancer cells.,” *Biomaterials*, vol. 33, no. 7, pp. 2345–50, Mar. 2012.

[19] A. A. Davis, M. J. Farrar, N. Nishimura, M. M. Jin, and C. B. Schaffer, “Optoporation and genetic manipulation of cells using femtosecond laser pulses.,” *Biophys. J.*, vol. 105, no. 4, pp. 862–71, Aug. 2013.

[20] N. L. Rosidi *et al.*, “Cortical microhemorrhages cause local inflammation but do not trigger widespread dendrite degeneration.,” *PLoS One*, vol. 6, no. 10, p. e26612, Jan. 2011.

[21] N. Nishimura, C. B. Schaffer, B. Friedman, P. S. Tsai, P. D. Lyden, and D. Kleinfeld, “Targeted insult to subsurface cortical blood vessels using ultrashort laser pulses: three models of stroke.,” *Nat. Methods*, vol. 3, no. 2, pp. 99–108, Feb. 2006.

[22] S. Kalies *et al.*, “Investigation of biophysical mechanisms in gold nanoparticle mediated laser manipulation of cells using a multimodal holographic and fluorescence imaging setup.,” *PLoS One*, vol. 10, no. 4, p. e0124052, Jan. 2015.

[23] R. Hobbie and B. Roth, “Transport in an Infinite Medium,” in *Intermediate Physics for Medicine and Biology SE - 4*, Springer New York, 2007, pp. 81–109.

[24] E. A. Schnell *et al.*, “Diffusion measured by fluorescence recovery after photobleaching based on multiphoton excitation laser scanning microscopy.,” *J. Biomed. Opt.*, vol. 13, no. 6, p. 64037, Jan. .

[25] Y. Du *et al.*, “Convection-driven generation of long-range material gradients.,” *Biomaterials*, vol. 31, no. 9, pp. 2686–94, Mar. 2010.

[26] P. L. McNeil, “Loss, Restoration, and Maintenance of Plasma Membrane Integrity,” *J. Cell Biol.*, vol. 137, no. 1, pp. 1–4, Apr. 1997.

[27] M. Terasaki, “Large Plasma Membrane Disruptions Are Rapidly Resealed by Ca2+-dependent Vesicle-Vesicle Fusion Events,” *J. Cell Biol.*, vol. 139, no. 1, pp. 63–74, Oct. 1997.

[28] R. Steinhardt, G. Bi, and J. Alderton, “Cell membrane resealing by a vesicular mechanism similar to neurotransmitter release,” *Science (80-.).*, vol. 263, no. 5145, pp. 390–393, Jan. 1994.

[29] L. V. Chernomordik, G. B. Melikyan, and Y. A. Chizmadzhev, “Biomembrane fusion: a new concept derived from model studies using two interacting planar lipid bilayers,” *Biochim. Biophys. Acta - Rev. Biomembr.*, vol. 906, no. 3, pp. 309–352, Oct. 1987.

[30] P. L. McNeil and M. Terasaki, “Coping with the inevitable: how cells repair a torn surface membrane.,” *Nat. Cell Biol.*, vol. 3, no. 5, pp. E124–E129, 2001.

[31] A. Draeger, R. Schoenauer, A. P. Atanassoff, H. Wolfmeier, and E. B. Babiychuk, “Dealing with damage: plasma membrane repair mechanisms.,” *Biochimie*, vol. 107 Pt A, pp. 66–72, Dec. 2014.

[32] D. Pilzer, O. Gasser, O. Moskovich, J. A. Schifferli, and Z. Fishelson, “Emission of membrane vesicles: roles in complement resistance, immunity and cancer.,” *Springer Semin. Immunopathol.*, vol. 27, no. 3, pp. 375–87, Nov. 2005.

[33] B. P. Morgan, J. P. Luzio, and A. K. Campbell, “Intracellular Ca2+ and cell injury: a paradoxical role of Ca2+ in complement membrane attack.,” *Cell Calcium*, vol. 7, no. 5–6, pp. 399–411, Dec. 1986.

[34] I. Walev, M. Hombach, W. Bobkiewicz, D. Fenske, S. Bhakdi, and M. Husmann, “Resealing of large transmembrane pores produced by streptolysin O in nucleated cells is accompanied by NF-kappaB activation and downstream events.,” *FASEB J.*, vol. 16, no. 2, pp. 237–9, Feb. 2002.

CHAPTER 5

IN VIVO OPTOPORATION

5.1 INTRODUCTION

Single cell genetic manipulation has the capability of significantly impacting the field of neuroscience. A longstanding challenge in neuroscience is targeted transfection of a single neuron *in vivo.* For example, by targeting channelrhodopsin to a single cell we could fire just that cell and observe how this impacted activity in nearby cells using calcium imaging. Such experiments provide a means to explore the local functional connectivity of neural circuits. Thus, Development of such a technique will expand our knowledge on the role of single neuron in terms of diseases manifestation, progression and regression, and functional analysis at circuit level.

An ideal technique will have high selectivity, specificity and non-toxicity, which will allow targeting a specific cell at a specific location while keeping the animal alive. For example, this will allow us to modify one, two or a few neurons with different genes and study the functional relationship between them. Similarly brain tumors, like glioblastoma can be investigated at initial cellular level by transfecting oncogenes into a single targeted cell *in vivo*. This will drive tumor development into targeted cells and will allow *in vivo* imaging of the earliest stages of tumor growth and of the cellular interactions that facilitate or, perhaps more interestingly, arrest tumor development.

In this chapter of the thesis, we discuss current *in vivo* transfection methods and the work done on establishing laser based transfection *in vivo***.** This includes optoporation in an acute mouse cortex using fluorescent dyes to record pore formation

and resealing dynamics. This work sets the stage for future development of a chronic *in vivo* model with DNA plasmid transfection.

5.1.1 Other *In vivo* Transfection methods

To achieve in vivo transfection there has been the development of knock out and transgenic animals. But these processes generally target a subpopulation of cells and are expensive, laborious and time intensive. For targeting only a single cell there have been studies using viral vectors. For example, retroviral and lentiviral vectors have been used to achieve multicolor RGB markings on a larger population of neurons, where each cell is distinguished by a specific hue[1]. However this technique is currently limited by computational modeling to identify and register each cells. Viral vectors are also limited in application by restrictions on insert and promoter sizes and possibility triggering an immune response[2], [3]. Non-viral plasmid DNAs are capable of overcoming immune responses and integrating larger inserts in comparison to viral vectors[4], but need robust transfection methods to be inserted into the cell.

Some of the challenges mentioned above have been addressed in part by other transfection methods such as electroporation, manual microinjection and modified patch clamp [5]–[9]. For example DNA vectors have been delivered via patch-pipette in mouse brain with expression lasting at least 7 days observed ex vivo [8]. Electroporation involves electric field application to disturb cell membrane's phospholipid bilayer to form hydrophilic pores through which exogenous material enters the cell.

Electroporation has been combined with patch clamp and shadow imaging for single neuron transfection and electrophysiology [10]–[12]. Recently, optogenetics and single cell electroporation were combined to express channelrhodopsin-2 in targeted cortical neurons [13]. However, single cell electroporation requires the pipette to be very close to the target cell and is technically challenging and low throughput[3].

Optoporation provides an alternative that has huge potential, as it is minimally invasive, sterile and has established itself as a successful technique for mammalian cells transfection. At present there is no method to the best of our knowledge that combines optoporation and single cell manipulation *in vivo*. Development of this technique opens the door to new avenues of research.

5.1.2 Femtosecond laser based *In vivo* Transfection

The literature on *in vitro* application uses an oscillator based femtosecond lasers for optoporation. There have been studies showing successful optoporation of neurons *in vitro* with naked DNA [14]. These lasers utilize high repetition rate laser and low pulse energy systems and operate slightly above the power for nonlinear imaging. These systems when applied to *in vivo* applications experience drawbacks with increasing tissue depth. These are scattering losses when pulse energies are low and thermal damage at the focal volume when pulse energies are increased[15]. This is a major drawback for future *in vivo* applications. To address this issue, high pulse energies are needed. We demonstrated *in vivo* optoporation at depths of 50-200 μm in mouse cortex

with a low rep rate 1Khz regenerative amplifier and 2-3 pulses at high pulse energies of 11-14nJ. This results in the formation of a high density plasma through avalanche and multiphoton ionization at the focusing volume. This is above the threshold for water breakdown. With 1 NA focusing this leads to ablative damage, material vaporization and pore formation on the plasma membrane. This ablative mechanism has been used to ablate blood vessels in mice cortex to model diseases[9,20,21].

The work done in this chapter helps in setting the stage and laying the foundation for chronic *in vivo* optoporation of single glia and neuron in a live animal model. In the following sections, we have used two techniques to establish the optoporation *in vivo*. We observed the inflow of 150kDa FITC dextran from outside environment the inside of cell. Additionally observed the outflow of dye in SR101 labeled astrocytes. Figure 5.2 illustrates the setup for the shadow imaging experiment.

5.2 METHODS

5.2.1 Animal preparation

In this study, we used male rats (3-8 months old), wild-type C57BL/6 mice, and 20-35 g in mass. At the start of the surgery, animal was anesthetized with 5% isoflurane in oxygen. During the surgery and imaging animal anesthesia was maintained at 1.5 - 2%. Bupivacaine (0.1 mL, 0.125%) was subcutaneously administered at the incision site on top of mouse head to provide local anesthesia. Glycopyrrolate (0.05 mg per 100-g

mouse) was intramuscularly injected to facilitate respiration. A 3-5 mm craniotomy was prepared over the parietal cortex. A 5-8 mm diameter, No. 1.5 glass cover slip (50201; World Precision Instruments) was glued to the skull using cyanoacrylate (Loctite) and dental cement (Co-Oral-Ite Dental Mfg Co.). Artificial cerebrospinal fluid (ACSF) was filled in the space between the exposed brain and cover glass. For maintaining mouse body temperature, a feedback controlled heating blanket (50-7053P; Harvard Apparatus) was used to maintain body temperature of 37.5° C. The animals were injected hourly with 5% (w/v) glucose in physiological saline (0.5 mL per 100-g mouse). These were acute experiments, animals were sacrificed at the conclusion of each imaging session. The care and experimental manipulation of our animals is approved by the Institutional Animal Care and Use Committee at Cornell University.

5.2.2 Two-photon excitation fluorescence microscopy

Imaging was done using a custom built four detection channel two-photon microscope. A Ti:Sapphire laser system laser (MIRA-HP; Coherent, Santa Clara, CA) with 100 fs pulse duration, 800 nm central wavelength, 10 nm FWHM bandwidth, and 76 MHz repetition was used. All imaging experiments used a Zeiss 20x magnification 1.0 NA upright microscope objective with water immersion (Zeiss, Thornwood, NY). Fluorescence collection was achieved using a 530-nm bandpass filter with 41-nm bandwidth. ScanImage (r3.8.1, Janelia Farm, USA) was used for image acquisition. Time lapse image acquisition for experiments was set at 3.15 frames/sec and 512x512

pixels. Image analysis and processing used custom written scripts in MATLAB (The MathWorks, Natick, MA) and ImageJ.

5.2.3 Regenerative amplifier for membrane ablation

A high pulse energy and low repetition rate regenerative Ti:Sapphire amplifier (Legend-USP; Coherent, Santa Clara, CA) was used for targeted optoporation of the cell membrane. It operated at 100 fs pulse duration, 790 nm central wavelength, 25nm FWHM bandwidth, and 1 kHz repetition rate. Neutral density filters, a fast mechanical shutter, a function generator, and an oscilloscope were applied to monitor and control the incident energy and number of pulses at each targeted site on the cell. One to three pulses were applied on the membrane target site. A polarizing beam splitter cube allowed to combine imaging and manipulation beam in the microscope setup and focussing the ablation beam in the centre of the imaging plane. The pulse energy at the objective was determined to be in the range of ~ 40nJ.

5.2.4 Labelling and setup

Post craniotomy, astrocytes are labeled with Sulforhodamine 101 (SR101) (S7635, Sigma Aldrich, St. Loius, MO), a red-emitting dye that labels exclusively astrocytes and not any other cell in the brain. 50ul of 125uM SR101 was microinjected about 100um below brain surface using a Nanoject II micropipette (Drummond Scientific Company, Broomal, PA). For shadow imaging 50ul of 150kDa FITC (Sigma

Aldrich, St. Loius, MO) was microinjected about 100um below brain surface using a Nanoject II micropipette (Drummond Scientific Company, Broomal, PA). The nanoject was attached to Patchstar micromanipulator (PatchStar Micromanipulator; Scientifica, East Sussex, UK) mounted on a Scientifica movable top plate for remote automated insertion into the cortex under the microscope. Once the needle was in the brain tissue, its imaged first under the 4x objective (Zeiss, Thornwood, NY) and then replaced by a 20x, water-immersed objective (Zeiss, Thornwood, NY).

5.3 RESULTS

5.3.1 Astrocyte targeting and characterization through outflow analysis

To determine successful cell perforation and resealing we analyzed the outflow of dye from a previously labeled cell. When perforated by femtosecond laser, living cells in the cortex show a drop in fluorescence. We use this to analyze the cell's viability and perforation post optoporation. For targeted cell transfection we chose astrocytes in an anaesthetized mouse. By a combination of topical application and microinjection of SR101 dye in mouse cortex, astrocytes fluoresced red under a two photon microscope. Post optoporation each astrocyte is categorized based on its change in fluorescence. As show in the Figure 5.1(a) – (c), Astrocytes were labeled red with SR101. Figure 5.1(b) shows three post optoporation profiles. The fluorescence of control astrocyte stays unchanged while the permeabilized astrocyte drops in fluorescence intensity, only to stabilize on effective resealing of cell membrane, and dead astrocyte experiences a

larger drop in fluorescence and disappears into the background. Figure 5.1(c) gives the energy range for most successful permeabilization. We obtain an energy range of 35-45 nJ to get about 50% transfection efficiency.

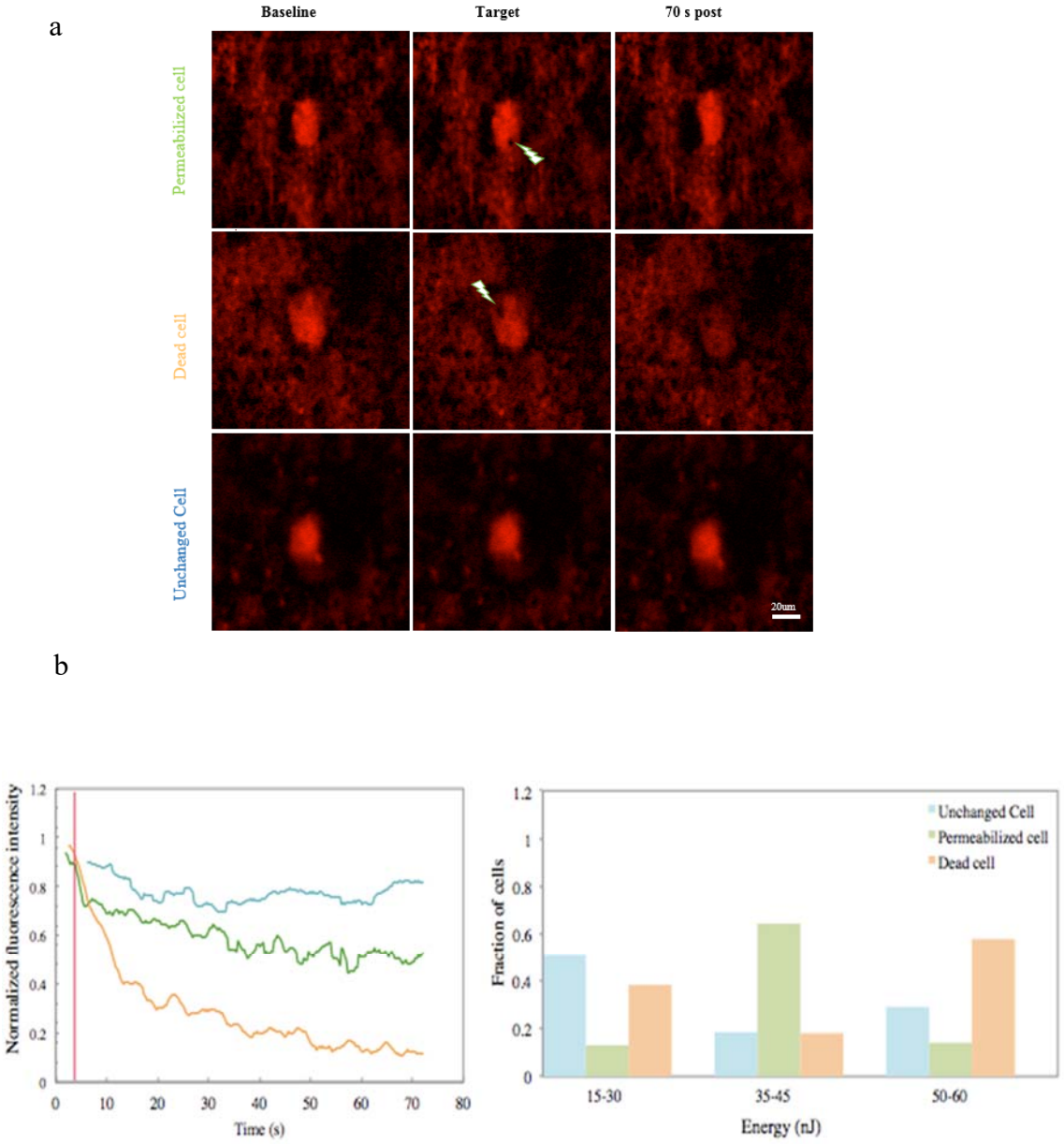

Figure 5.1 Outflow of SR101, fluorescently labeled dye in the astrocytes cytoplasm. a) Exemplary fluorescence images for astrocytes in different cases of viability. Scale bar is 20um. b) Normalized fluorescence intensity profiles of cells as unchanged (blue), permeabilized (green) and dead cell(orange). c) Energy as a function of fraction of cells that were peramibilized. At 35-45 nJ maximum transfection is obtained.

5.3.2 Inflow analysis with shadow imaging

We analyzed inflow experiments by examining the entry and rise of fluorescence of dye in the cell from the extracellular space. We used shadow imaging to visualize single cells deep in mouse cortex. It is a technique where membrane impermeable fluorescent dye is microinjected into cortex to stain the extracellular space in a small area, the cells in this area do not get labeled and when imaged appear as a negative image (shadow) in a bright background. This technique has been used with electroporation and patch clamping[6], [19].

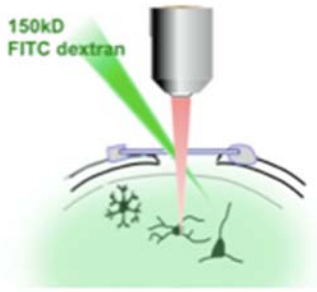

Figure 5.2 Illustrative diagram of injection of 150kDa FITC dextran into mouse cortex for shadow imaging and single cell optoporation.

In this chapter, for the first time to our knowledge, we have applied shadow imaging to optoporation technique for single cell manipulation. Here, we microinject 150 kDa FITC dextran into mouse cortex that makes the extracellular space fluorescence green and cells appear as dark negative image. Cells are visually identified based on

their somatodendritic structure provided background contrast is strong, this becomes a challenge for extracellular space labeling. In this study we do not identify the cell type. As shown in figure 5.3(a), we observe two cells, one is targeted and other is control. As the dextrans enter the cell, we distinctly see an increase in fluorescence intensity of the targeted cell and after about 20seconds saturates indicating pore closure, as shown in Figure 5.3(b) where deltaF/F0 is plotted against time,. We also notice that the control cell remains unaffected. In Figure 5.3(c) we have a dead cell, indicated by its fluorescence increase followed by an abrupt drop. Initially when targeted, pore gets created leading to inflow of dextrans, but over time the fluorescence intensity drops significantly. We analyze deltaF/F0 for both pore and cell as shown in Figure 5.3 (d) which points to a dead cell.

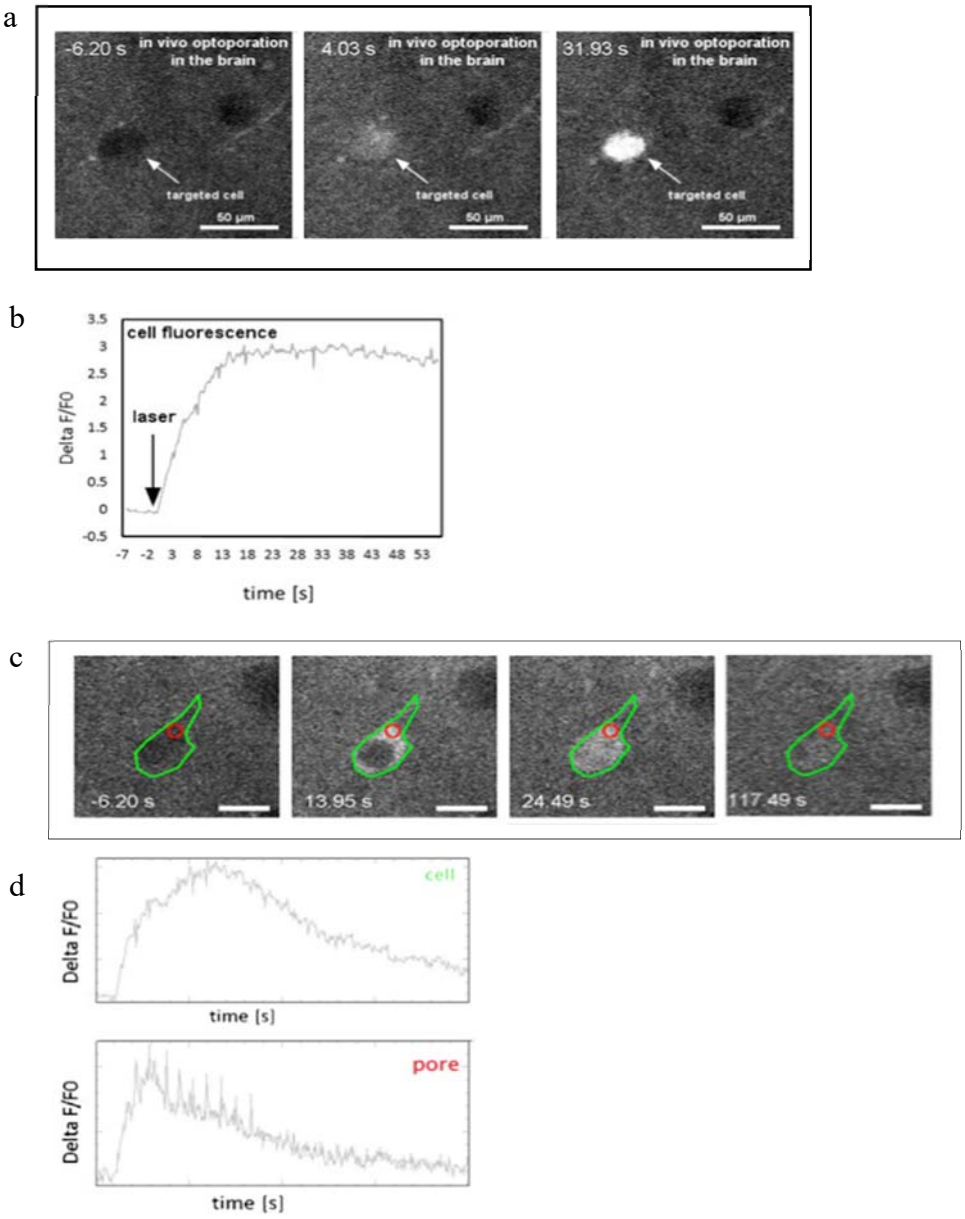

Figure 5.3 Inflow of 150 kDa FITC dextran. a) and b) Viable cell profile, fluorescently labeled dye enters the cell and reaches saturation. c) and d) Dead cell profile, the dextrans enter the cell cytoplasm then nucleus and then loses its fluorescent intensity.

5.4 CONCLUSION

In these experiments we have successfully established the feasibility of single cell *in vivo* optoporation. The current data provides a working model for single cell *in vivo* optoporation and its parameters are in agreement with the dynamics and parameters we established with *in vitro* optoporation in the previous chapters. This sets the stage for future exploration and establishment of *in vivo* optoporation as a tool for single cell genetic manipulation. For future experiments, a chronic long term re-openable craniotomy will enable repeated optoporation of individual cells. Microenvironment response to single cell manipulation can be visualized and explored by using transgenic mice where specific cell populations are labeled. Further calcium response in astrocytes and neurons in normal and diseased states can be analyzed. It also opens up avenues for delivery and transfection of quantum dots, SiRNA and plasmid DNA. Another alternative is using naked DNA which unlike viral vectors have no immune response from the host. This technique also has the potential to study early stages of tumor growth and arrest from a single cell stage. Additionally, cell- cell interactions and functional connectivity studies can be explored with this technique. Ultimately this approach is dependent on many factors including operator skill, brain region, animal age, cell microenvironment and efficient equipment. The work done so far in this chapter with developing successful inflow and outflow optoporation experiments in mouse cortex sets the stage for *in vivo* single neuron optoporation.

REFERENCES

[1] D. Gomez-Nicola, K. Riecken, B. Fehse, and V. H. Perry, "In-vivo RGB marking and multicolour single-cell tracking in the adult brain.," *Sci. Rep.*, vol. 4, p. 7520, Jan. 2014.

[2] P. Bigey, M. F. Bureau, and D. Scherman, "In vivo plasmid DNA electrotransfer.," *Curr. Opin. Biotechnol.*, vol. 13, no. 5, pp. 443–7, Oct. 2002.

[3] J. De Vry *et al.*, "In vivo electroporation of the central nervous system: a non-viral approach for targeted gene delivery.," *Prog. Neurobiol.*, vol. 92, no. 3, pp. 227–44, Nov. 2010.

[4] K. L. Douglas, "Toward Development of Artificial Viruses for Gene Therapy: A Comparative Evaluation of Viral and Non-viral Transfection," *Biotechnol. Prog.*, vol. 0, no. 0, pp. 0–0, Mar. 2008.

[5] K. Haas, W. C. Sin, A. Javaherian, Z. Li, and H. T. Cline, "Single-cell electroporation for gene transfer in vivo.," *Neuron*, vol. 29, no. 3, pp. 583–91, Mar. 2001.

[6] K. Kitamura, B. Judkewitz, M. Kano, W. Denk, and M. Häusser, "Targeted patch-clamp recordings and single-cell electroporation of unlabeled neurons in vivo.," *Nat. Methods*, vol. 5, no. 1, pp. 61–7, Jan. 2008.

[7] K. Nolkrantz *et al.*, "Electroporation of single cells and tissues with an electrolyte-filled capillary.," *Anal. Chem.*, vol. 73, no. 18, pp. 4469–77, Sep. 2001.

[8] E. A. Rancz, K. M. Franks, M. K. Schwarz, B. Pichler, A. T. Schaefer, and T. W. Margrie, “Transfection via whole-cell recording in vivo: bridging single-cell physiology, genetics and connectomics.,” *Nat. Neurosci.*, vol. 14, no. 4, pp. 527–32, Apr. 2011.

[9] N. N. Kasri, E. Govek, and L. Van Aelst, “Characterization of Oligophrenin-1, a RhoGAP Lost in Patients Affected with Mental Retardation: Lentiviral Injection in Organotypic Brain Slice Cultures,” in *Methods in enzymology*, vol. 439, 2008, pp. 255–266.

[10] E. Neumann, M. Schaefer-Ridder, Y. Wang, and P. H. Hofschneider, “Gene transfer into mouse lyoma cells by electroporation in high electric fields.,” *EMBO J*, vol. 1, no. 7, pp. 841–845, 1982.

[11] J. C. Weaver and Y. A. Chizmadzhev, “Theory of electroporation: A review,” *Bioelectrochemistry Bioenerg.*, vol. 41, no. 2, pp. 135–160, Dec. 1996.

[12] K. Haas, W.-C. Sin, A. Javaherian, Z. Li, and H. T. Cline, “Single-Cell Electroporationfor Gene Transfer In Vivo,” *Neuron*, vol. 29, no. 3, pp. 583–591, Mar. 2001.

[13] B. Judkewitz, M. Rizzi, K. Kitamura, and M. Häusser, “Targeted single-cell electroporation of mammalian neurons in vivo,” 2009.

[14] M. Antkowiak, M. L. Torres-Mapa, E. C. Witts, G. B. Miles, K. Dholakia, and F. J. Gunn-Moore, “Fast targeted gene transfection and optogenetic modification of single neurons using femtosecond laser irradiation.,” *Sci. Rep.*, vol. 3, p. 3281, Jan. 2013.

[15] A. A. A. Davis, M. J. J. Farrar, N. Nishimura, M. M. M. Jin, and C. B. B. Schaffer, "Optoporation and genetic manipulation of cells using femtosecond laser pulses.," *Biophys. J.*, vol. 105, no. 4, pp. 862–71, Aug. 2013.

[16] C. Schaffer, N. Nishimura, E. Glezer, A. Kim, and E. Mazur, "Dynamics of femtosecond laser-induced breakdown in water from femtoseconds to microseconds," *Opt. Express*, vol. 10, no. 3, p. 196, Feb. 2002.

[17] N. L. Rosidi *et al.*, "Cortical microhemorrhages cause local inflammation but do not trigger widespread dendrite degeneration.," *PLoS One*, vol. 6, no. 10, p. e26612, Jan. 2011.

[18] N. Nishimura, C. B. Schaffer, B. Friedman, P. S. Tsai, P. D. Lyden, and D. Kleinfeld, "Targeted insult to subsurface cortical blood vessels using ultrashort laser pulses: three models of stroke.," *Nat. Methods*, vol. 3, no. 2, pp. 99–108, Feb. 2006.

[19] B. Judkewitz, M. Rizzi, K. Kitamura, and M. Häusser, "Targeted single-cell electroporation of mammalian neurons in vivo," *Nat. Protoc.*, vol. 4, no. 6, pp. 862–869, May 2009.

[20] M. D. Brown, A. G. Schätzlein, and I. F. Uchegbu, "Gene delivery with synthetic (non viral) carriers.," *Int. J. Pharm.*, vol. 229, no. 1–2, pp. 1–21, Oct. 2001.

CHAPTER 6

VOLUMETRIC IMAGING OF CONVECTION ENHANCED DRUG DELIVERY

This chapter is the manuscript for a future paper. That will be tentatively titled as follows

Gadamsetty, P* Rosch, J* Schaffer, CB and Olbricht, WB Volumetric imaging of convection enhanced drug delivery in rat cortex, 2017

6.1 ABSTRACT

A wide variety of therapeutics of varying sizes have been delivered using Convection-Enhanced Delivery (CED) from small molecules to drug-laden nanoparticles. This study focuses on real time imaging and transport dynamics of different sized nanoparticles in the brain interstitium and the perivascular space (PVS).

The structure of the brain interstitium restricts drug penetration but perivascular spaces provide alternative transport routes. Drug size, infusion volume and coverage area in the brain have a significant impact on therapeutic potential. Optimization and analysis of transport mechanisms for convection enhanced drug delivery and determining the role of drug size on infusion volume are important prerequisites for developing effective drug delivery systems. We developed a fast scanning, real time volumetric imaging platform to study transport of nanoparticles and liposomes in the rat cortex *in vivo* with high temporal and spatial resolution. Fluorescent polystyrene beads of sizes 20, 40 and 100 and 200nm, and liposomes of sizes 50, 100, and 200nm are infused at 0.2 μl/min into the cortex at 100-300 μm depth. With smaller particles being in the same size range of extracellular space pores (38-64nm), we observe that the distribution volume is higher and particles are found throughout the parenchymal region. Whereas for larger sized particles, distribution area is smaller but highly concentrated and occupies more of perivascular spaces along blood vessels. Solid nanoparticles face resistance to motion 10 times more in the interstitium than in perivascular spaces, but this difference is decreased for liposomes. Understanding size

dependent transport mechanisms is critical to design and optimization of systems that deliver drug-laden nanoparticles and liposomes in the brain.

6.2 INTRODUCTION

The big challenge with delivering drugs into the brain is the blood brain barrier (BBB). The BBB only readily allows the entry of small somewhat lipophilic drugs greatly limiting the range of therapeutic options. Direct infusion of drugs into the brain circumvents the BBB, but drug distributions are then determined by the transport from the infusion site through the tissue. Transport dynamics in brain tissue vary due to many factors including disease, inflammation, grey and white matter regions, perivascular spaces, parenchyma areas and brain fluid dynamics.

The flow of the fluids in the brain cannot be understood without understanding vascular anatomy. The brain cortical surface has cerebral arteries extending down as pial arteries and then as penetrating arterioles into the brain parenchyma. The pia mater forms an outer layer around the arteries as they enter the brain parenchyma [1]. The brain consists of mainly three fluid components besides blood. The cerebrospinal fluid (CSF) (10%), interstitial fluid (ISF) (10-12%) and the intra cellular fluid (60-68%). The CSF is produced in the choroid plexus and completely penetrates into the brain parenchyma. It enters via peri-arterial spaces, flows into the spaces along capillaries, then into peri-venous spaces and finally exits out into the into the lymphatic system [2], [3]. These spaces are termed as Virchow-Robin spaces at the beginning of the

penetrating arterioles and then as the perivascular spaces. Their widths range from 5-20 microns [4]. In comparison, the extracellular space (ECS) matrix has pore sizes in range of 38-64 nm in rodents[5]. There is an outer bounding wall comprising of astrocytic end feet, these have clefts of about 50 nm, so particles sized less than that can transport directly into the parenchyma while flowing in the perivascular spaces. [3].

6.2.1 Perivascular and parenchymal transport

Many studies have focused on how infusate distribution occurs in the brain with tracers, liposomes and viral vectors[1], [6]–[8]**.** Majority of drug distribution though parenchymal transport is in the extracellular space (parenchyma) and through perivascular transport is along the blood vessels (perivascular spaces). There is a growing literature emphasizing the potential of perivascular spaces in drug delivery and as therapeutic targets for management of diseases. For example, in metastasis glioma cells have been found to migrate several centimetres away from the central tumour site into healthy tissue. Despite surgical resection, these migrated malignant cells cause tumor again[9]. Interestingly, 80% of glioma tumours developed and progressed in the perivascular spaces along the blood vessels. In Alzheimer's disease, aging causes deposition and accumulation of protein aggregates such as b-amyloid peptides in the perivascular pathways. Large accumulation can cause blockages in the pathways and can impair regular neurological functions[3]. Other diseases like Parkinson's, vascular dementia, traumatic brain injury also depend on the effective functioning of the perivascular spaces. Perivascular spaces have been found to have higher hydraulic

conductivity for all particles. Injected tracers achieved quick and large distribution volume throughout the perivascular spaces[10]–[12]. Recently more focus has been placed on the routes taken by the solutes. In 2008, Carare et.al found clearance for soluble tracers like fluorescently labelled dextrans was along para-arterial routes[13]. In contrast, Nedegaard et al., identified the glymphatic system which comprises of para-venous routes for interstitial solute clearance and para-arterial routes for perivascular CSF recirculation [3], [4]. In 2006 the term perivascular pumping got introduced for the mechanism of blood vessel pulsations via heartbeat that acts as a pump and causes the infusate to move further into the perivascular spaces [14]. Rats with artificially lowered heart rate and blood pressure had comparatively smaller distribution volume of infused liposomes. Wang and Olbricht theoretically analysed that pumping mechanism of blood vessels facilitates infusate and fluid flow in the perivascular spaces[15]. Lately, with ultra-fast magnetic resonance encephalography it was found that cardiovascular, respiratory and vasomotor pulsations together affect CSF flow dynamics in the brains[16] .

6.2.2 Diffusion Method

One of the widely used method for drug delivery across BBB is diffusion. Westphal et al., packed chemotherapy drug carmustine (BCNU) in biodegradable wafers (Gliadel wafers) into the post-surgery tumor resection cavity to deliver drug over time [17]. They observed that the drugs did not travel deep and caused more complications. In diffusion, the distance covered is proportional to the square root of

time of infusion. In addition, drug infused leaks into non-targeted sites, cannot diffuse deep and constantly cleared up by CSF. Pre-clinical trials show half-life of drugs in the tissue is about 7 hours[1]. Because diffusion does not lead to deep penetration and provides limited control over drug distribution its utility for therapeutic applications is limited.

6.2.3 Convection Enhanced Delivery Method

In 1994, RH Bobo et al., introduced convection enhanced technique for intra-parenchymal drug delivery *in vivo* [18]. Convection enhanced delivery (CED) is an acute neurological drug delivery technique where microcatheters or microneedles are inserted directly into brain parenchyma to infuse drugs. By externally controlling flow rate, hydrostatic pressures gradient establish at the tip of needle, which in turn, cause drug infusion directly into the brain by bypassing the blood brain barrier. Moreover, volume of distribution (V_D) increased linearly with volume of infusion (V_I) [1], [18], [19]. Convection enhanced drug delivery systems are more effective in delivering size restricted drugs across the blood brain barrier, distributing therapeutically relevant drug concentrations, minimizing leakages in non-targeted areas, achieving larger distribution areas, and minimizing systemic exposure. It has the therapeutic potential for various neurological and neuro-oncological diseases. Despite extensive advances, clinical trials have failed to establish CED as a successful method of treatment. The PRECISE trial [20]–[22] for glioblastoma found that drug distribution was both unpredictable, different

amongst the patients, and therapeutically relevant concentrations of drugs were not found at the tumour site.

Thus, it is important to understand drug distribution and transport dynamics of particles in both parenchyma and perivascular regions to build effective treatments and optimize CED. Moreover, real time monitoring of drug distribution will aid researchers and neurosurgeons with a dynamic understanding of drug penetration and retention in the tissue and in turn effectively improve them. Currently, magnetic resonance imaging (MRI) is used for such real time monitoring studies by taking periodic images of drug distribution. In rats and primates, intraoperative MRI imaging of CED for viruses, liposomes has been done to image both placement of cannula and to calculate V_D [23]–[26]. Since perivascular spaces are in the range of microns, the MRI is not capable of resolving flow dynamics at those resolutions. This further complicates predicting and understanding CED drug distribution in both the perivascular and extracellular/interstitial spaces. Another leading imaging technique in this area is two-photon microscopy. It is capable of high spatial and temporal resolution images when it comes to real time observation of convection-enhanced particle flow dynamics.

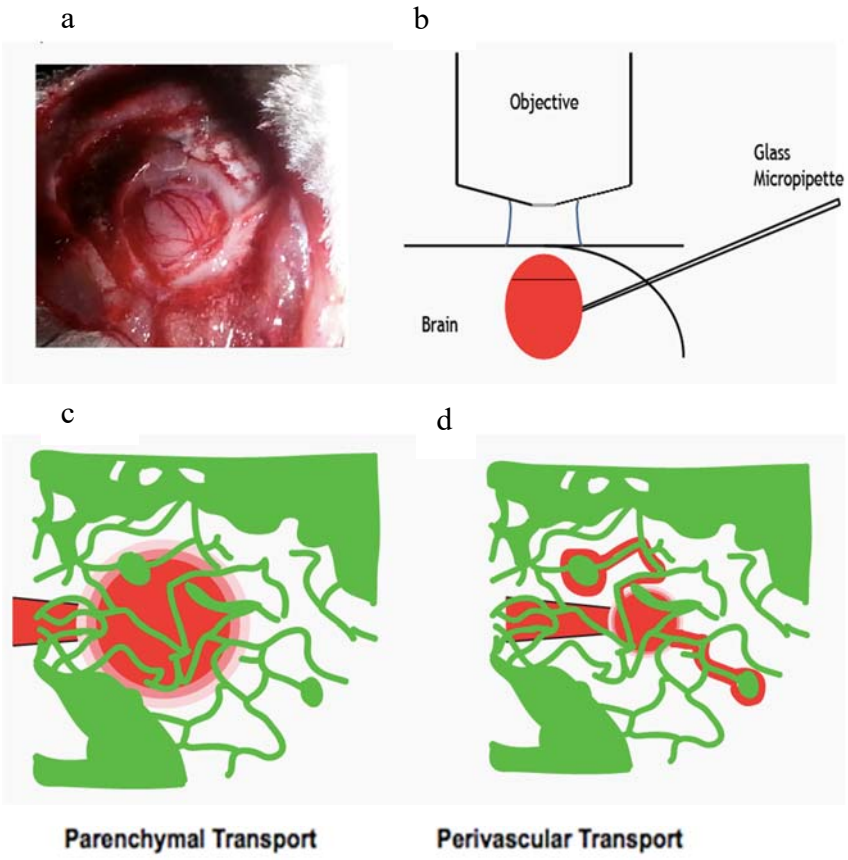

Figure 6.1 Experimental platform and drug transport profiles in the brain parenchymal region and perivascular region. a) Rat cortex with 8mm wide craniotomy and glass coverslip. b) Illustrative diagram of experimental platform with the needle in the cortex and rat with an open craniotomy placed under the objective of a two-photon excitation microscope. c) Parenchymal transport has primarily drug distribution in the extracellular space and perivascular transport occurs along the blood vessels.

In this direction, we have previously demonstrated[27] real-time two-photon flow of nanoparticles in perivascular spaces were the highly preferred route for large nanoparticles in the tissue. These results suggested that two-photon excitation microscopy *in vivo* has higher resolution to study nanoparticle flow dynamics in more detail in real time. CED with two-photon volumetric distribution in real time from the

needle tip to the outer surface and deeper areas has a lot of potential. It has not been documented or studied to the best of our knowledge. In this paper, we have built a custom real-time volumetric imaging platform for high-resolution imaging of nanoparticles and liposomes in rat cortex. Figure 6.1 illustrates experimental platform and the drug distribution in these spaces of parenchyma and perivascular. Further, we have characterized the transport mechanics of different sized nanoparticles and liposomes in particular in the perivascular and parenchymal spaces of the brain. Further studies in this direction can leads to more optimized, precise and predictable outcomes of CED in clinical trials.

6.3 METHODS

6.3.1 Nanoparticle and Liposome Preparation

Carboxylate-modified red-orange fluorescent nanoparticle stock solutions (20, 40, 100 and 200 nm Fluospheres, Life Technologies, Grand Island, NY) were sonicated for 15 min prior to dilution to 0.1 wt% solids in a solution of bovine serum albumin (BSA, Sigma-Aldrich, St. Louis, MO) in phosphate buffered saline. Nanoparticle solutions were allowed mixing on laboratory rocker at low speed for 4hrs. BSA conjugation to carboxylate-modified surface allows for reduction of surface charge of polystyrene nanoparticles, reducing non-specific binding of the solids upon infusion into rodent brain. Fuschia-colored suspensions of 50, 100, and 200 nm liposomes were procured from Avanti Polar Lipids, Inc. These liposomes were of molar ratio of 55:44:1 DOPC: cholesterol: Texas Red DHPE. The formulation involved extrusion through appropriate filters to form liposomes of the analogous size. The liposomes were suspended in buffer solution containing 10 mM HEPES, pH 7.4, 150 mM NaCl, and 1 mM $MgCl_2$, and further diluted to 10^{11}-10^{12} particles/mL. Size and surface charge of the nanoparticles were determined before and after BSA incubation (Zetasizer Nano, Malvern Instruments Ltd., UK). The measured sizes and zeta potentials of the particles before and after BSA conjugation are summarized in Table 6.1. Dynamic light scattering (DLS) characterization techniques are sensitive to the presence of large particles being present in the solutions. Large particles can change the average diameter measured by the Zetasizer, which might explain the larger than anticipated average particle diameter,

both before and after BSA conjugation. The hydrodynamic diameter of BSA is ~7 nm and its presence on on both sides of the polystyrene bead explain the growth in the diameter of the particles when conjugated with BSA. Moreover, BSA conjugation reduces the zeta potential of the particles, which in turn reduce non-specific binding once infused into the brain parenchyma during these experiments.

For liposomes, the polydispersity index (PDI) indicates presence of a large range of particles in the suspension, with the average heavily influenced by the presence of low amounts of larger particles in the suspension. Further investigation into zetasizer data indicated that for the 50 nm particles, over half were in the range of 50-100 nm. While the 50 and 100 nm suspensions of liposomes were not all of an ideal size, a large proportion of the particles were of an appropriate size to label these suspensions in such a manner. The results of the infusions are thus influenced by the distribution of particles present in the suspension, but this is largely unavoidable for this type of particle used.

For co-infusion experiments, 1 wt% Cascade Blue dextran in phosphate buffered saline solution was mixed with the 0.1 wt% 200 nm nanoparticle solution in a 1:4 ratio.

Table 6.1 Average particle diameter, polydispersity index, and zeta-potentials for all particles used. Stock solutions prior to surface modification are also shown. SEM shown for particle diameter and zeta-potential. All values were measured in triplicate, giving these averages and SEM.

Particle	average Z-ave (nm)	SEM Z-ave (nm)	average PdI	average ZP (mV)	SEM ZP (mV)
50 nm lipo	137.3	2.417	0.181	-4.1	0.538
100 nm lipo	186.5	4.911	0.248	-3.5	0.265
200 nm lipo	246.5	11.145	0.294	-2.7	0.347
20 nm stock	29.1	0.419	0.080	-30.5	1.479
20 nm bsa	50.6	0.408	0.248	-10.5	0.450
40 nm stock	49.8	0.505	0.0426	-32.3	2.771
40 nm bsa	75.4	0.504	0.121	-11	0.346
100 nm stock	108.9	0.688	0.012	-38.3	0.338
100 nm bsa	131.3	0.845	0.0173	-11.2	1.028
200 nm stock	179.9	1.637	0.0176	-34.1	2.030
200 nm bsa	207.6	0.536	0.00933	-10.1	0.309

6.3.2 Infusion Setup Preparation

Adult male Sprague-Dawley rats (weighing 250-450 g) were anesthetized with isoflurane inhalation. Animals were secured in a stereotactic frame and an incision was made in the skin along the dorsal midline. Skin and muscle tissue were excised to reveal a ~3 cm section of the skull. A dental drill was used to open a ~1 cm circular craniotomy, exposing the brain from near the midline to the arch on the right side of the skull. A 30 gauge needle was used to make a small incision in the dura, and a fine hook was then used to pull back the dura to the outer portions of the craniotomy. Once bleeding near the craniotomy had ceased, fluorescein isothiocyanate (FITC) conjugated to 2-MDa dextran (Sigma-Aldrich, St. Louis, MO) was administered directly to the bloodstream *via* tail vein injection. FITC, once in the bloodstream, labels the blood plasma, allowing for visualization of the vasculature in the brain using 2PEF. A glass coverslip was placed

over the craniotomy and fixed to the skull using dental cement. All animal procedures were performed in accordance with the Cornell University Institutional Animal Care and Use Committee guidelines and regulations.

Animals were transferred to the imaging setup, where they are placed on a motorized stage beneath the 2PEF microscope objective. A 4X objective (Zeiss, Thornwood, NY) was used to locate the craniotomy. Using a micromanipulator, a fixed rod with a micropipette of outer diameter ~10-20 μm was brought into the field of view above the coverslip. The pipette was then retracted, lowered, and inserted parallel to the surface of the brain at a depth of ~100 to 400 μm. The pipette could be seen under 2PEF due to the presence of fluorescently labeled particles in the solution, which was primed through the needle tip. The vasculature and nanoparticles could be identified in separate channels on the imaging computer. Once the needle was in the tissue, the 4X objective was replaced by a 20X, water-immersed objective (Zeiss, Thornwood, NY).

6.3.3 Imaging Experiment

2PEF images were taken on two-channel microscope of local design using 100 fs duration pulses from a 76 MHz repetition rate Ti:sapphire laser system (Mira-HP, Coherent, Santa Clara, CA) pumped by a continuous wave laser (Verdi-V18, Coherent, Santa Clara, CA). Excitation wavelength was set to 800 nm, which allowed for excitation of both the FITC and the red-orange nanoparticles. Fluorescence collection was achieved using a 610-nm and 530-nm bandpass filter. ScanImage (r3.8.1, Janelia

Farm, USA) was used for image acquisition. Pipette movement done with use of a 4x air objective (Zeiss, Thornwood, NY). High magnification images were captured with a 1.0 NA, 20x water immersion objective (Zeiss, Thornwood, NY).

Infusions were made at a flow rate of 0.2 μL/min using a PHD-2000 constant flow infusion pump (Harvard Apparatus). While pumping, the motorized stage was used to move the animal and micromanipulator in an oscillatory motion beneath the objective. The imaging plane would stay fixed in space, but the vessels and infusion cloud being imaged would change based on the height of the stage relative to the objective. 512 x 512 pixel images were captured at a frame rate of 3.15 frame per second. This resolution and frame rate were previously determined to be sufficient for viewing transport at adequate spatial and temporal resolution. The animal would be continually moved toward and away from the microscope objective until the infusion cloud had reached the edge of the field of view. At this point little to no information could be gathered form the images, and thus it was not necessary to continue recording. Multiple infusions were performed within a single animal. The edge of each infusion cloud could be seen, meaning each subsequent infusion needed to be done where the field of view would not pick up any residual fluorescence from a previous cloud. Infusions were done until there was no more visible space, the imaging quality degraded too much, or the animal died. If the animal was still alive at the end of imaging, pentobarbital was administered *via* intraperitoneal injection to induce euthanasia.

6.3.4 Image Analysis

2PEF imaging files were exported as multi-image tagged image file format (TIFF) stacks for analysis in ScanImage (r3.8.1, Janelia Farm, USA) and MATLAB (The MathWorks, Natick, MA). In ImageJ, image stacks were loaded in one at a time. A 1-pixel 3D median filter was used to remove noise from the stack. From here, the two channels were combined into a composite image for each depth within the brain. Brightness and contrast were adjusted for viewing and data analysis. Perivascular routes and parenchymal cloud growth could be assessed using these image stacks. In MATLAB, filtered image stacks were loaded in one at a time. A threshold was calculated based on image histograms in order to remove any background noise. From here, custom code was used to calculate the volume of distribution and surface area of the cloud for each sampling of the cloud.

6.4 RESULTS

6.4.1 Particle Infusions

In order to gain a fundamental understanding of the movement of nanoparticles and liposomes injected during a CED-like infusion, we continuously imaged the cloud of infused material over the course of the infusion. This allowed us to evaluate numerous aspects of infusion with unparalleled temporal (~30 s per volume sample) and spatial (~2.5 μm^3 voxel size) resolution. We found that these particles of all sizes and types

(and fluid tracers) would travel preferentially along particular perivascular routes, and the presence of these perivascular spaces greatly influences the morphology of the infusion cloud. Furthermore, velocities could be estimated for a large number of perivascular pathways, which allows for direct comparison to parenchymal transport, and its importance to drug delivery during a CED-like infusion. Our technique can accurately track the progression of the growth of the cloud with incredible detail, which is necessary for understanding the particle dynamics at this scale.

6.4.2 Larger particles Vd dependent on presence of perivascular spaces (Cloud Morphology for rigid polystyrene beads)

To understand distribution of different sized particles, we studied volumetric time lapse images of the growing infusion cloud as shown in Figure 6.2 and 6.3 in an anesthetized rat cortex. For the smallest particle size, 20 nm, the infusion cloud grew as a sphere in the parenchyma indicative of isotropic growth. Perivascular routes are occupied by the infused 20 nm particles, but due to their small size, growth rate of the cloud in parenchyma is comparable to the movement of particles in the PVS. For larger sized particles (40, 100, and 200 nm), the growth of the infusion cloud was primarily influenced by the presence of perivascular routes, which leads to a combination of initially hindered isotropic growth in the parenchyma and anisotropic growth along the perivascular spaces. The larger particles sizes approach and exceed the average pore size (38-64 nm) of the extracellular space (ECS), experiencing hindrance to their movement. The presence of local PVS leads to preferential movement of the particles

toward these high-conductance fluid pathways. Moreover, we observed that for larger particles such as 200 nm, the path is restricted to perivascular spaces only.

Thus, distribution volume in the neural tissue decreases with increasing nanoparticle sizes and the perivascular spaces along blood vessels provide higher conductivity pathways for all particles.

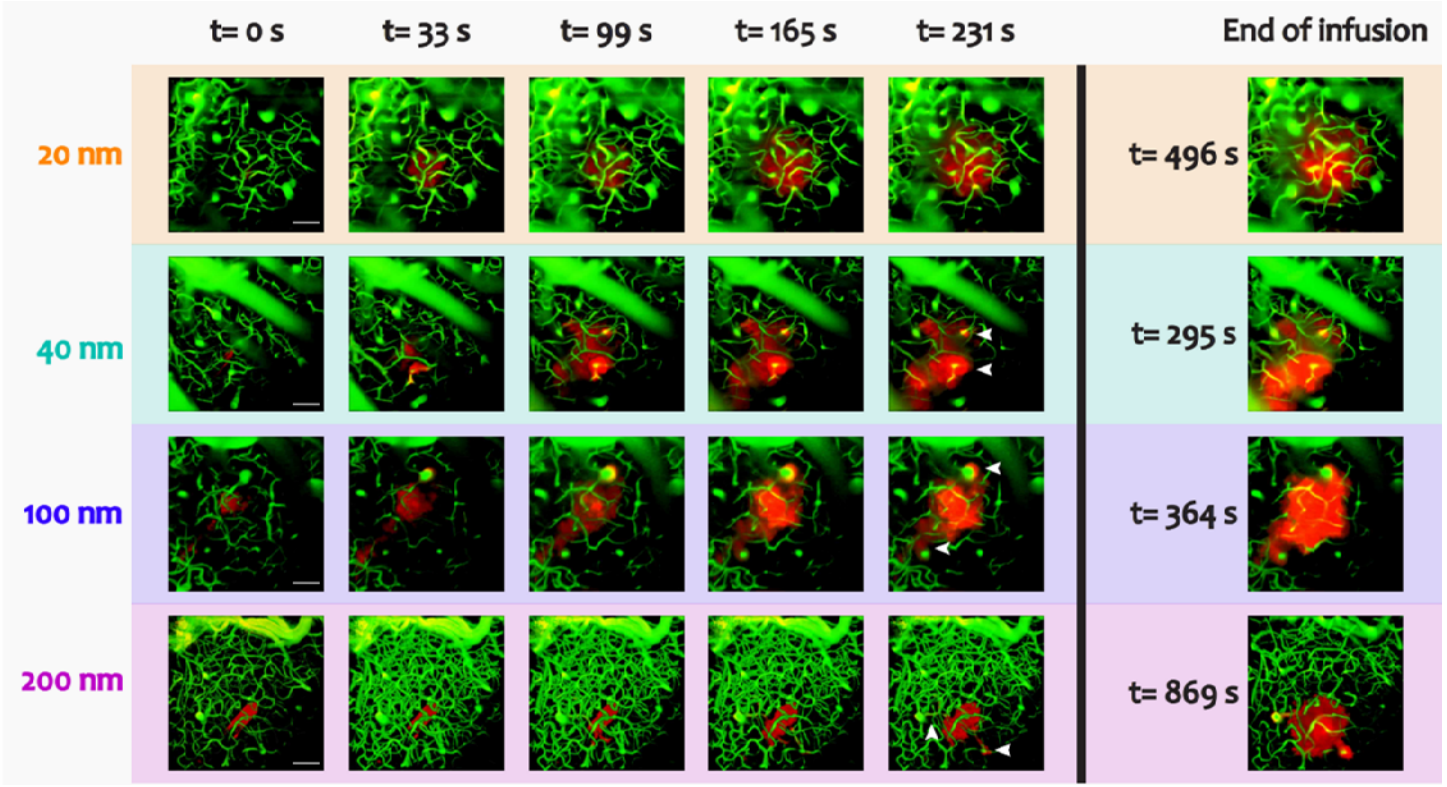

Figure 6.2 Time lapse imaging of particle infusion cloud growth in rat cortex. Perivacular routes influence infusion cloud growth rate for larger sized nanoparticles. Distribution volume and time is lesser for larger sized nanoparticles. Vasculature labeled with FITC-dextran (green) and nanoparticles labeled in (red)

6.4.3 Volume of distribution to infusion ratio increases with particle flexibility

Figure 6.4 shows the volume of distribution to volume of infusion ratio for infusion of each liposomes and polystyrene beads used. In the case of liposomes, 50 nm sized liposomes showed significantly higher Vd/Vi than 100nm and 200nm sized liposomes. Similarly in the case of polystyrene beads, Vd/Vi showed a relatively steep drop after 20nm and 40nm beads. This demonstrates again that the ECS pore size plays a role in thresholding the movement of particles as the average pore size of 38-64nm is approached and exceeded. On comparison of liposomes and polystyrene beads, it clearly shows that liposomes have about three to eight times higher average V_D/V_I ratio than similarly size beads. This indicates that higher flexibility and less rigidity in the construction of the nanoparticle can significantly reduce hindrance to its flow within the parenchyma.

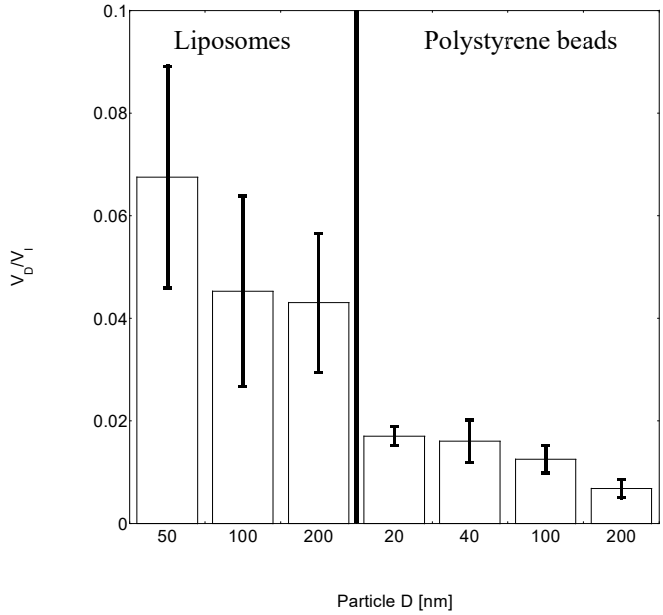

Figure 6.4 Volume of distribution to Volume of infusion compared against particle size and type, liposomes had larger Vd/Vi because of their highly flexible structure. All particles experience hindrance to their movement, but it increases with rigid structure and when size approaches ECS pore size. 200nm nanoparticles have the smallest Vd/Vi in comparison to 100nm liposomes. Sample size, from left starting at 50 nm liposome, to right ending at 200 nm bead, is: n = 10, 6, 9, 7, 5, 9, 10.

6.4.4 Cloud growth in the parenchyma decreases over time

To understand nanoparticle transport in the parenchyma, we focused on radial growth and velocity behavior across all the infused nanoparticles. All particles upon entering the brain tissue, experiences hindrance to their movement through the ECS between cells. The initial velocity declines sharply and cloud radius increases. This radial and velocity behavior over time in the parenchyma is shown for each particle size and type in Figure 6.5. Based on cloud radius growth, it is observed that for a given time point, the 20 and 40 nm beads are capable of reaching larger distances in the parenchyma than the 100 and 200 nm sizes. Moreover, smaller bead sizes do not show as stark of a plateauing behavior if the infusion were to continue longer. The larger beads display a

plateauing behavior around 10 mins, indicating that continual pumping of nanoparticle solution into the parenchyma at a fixed flow rate does not yield additional appreciable cloud growth. The liposomes show similar behavior to the beads, smallest liposomes of 50 nm sizes, did not display plateauing behavior, and in theory could have shown much larger cloud sizes given longer infusion times. This would not be possible to observe within the constraints of our system without losing resolution to observe perivascular behavior.

All of the particle sizes and types displayed large drops in velocity after initial times. We observed that after the first 30 to 60s of infusion, the particles were moving at less than 1 μm/s speeds along the edge of the cloud. This continued to drop with increasing infusion time. The smaller particle sizes maintained a higher cloud front velocity for longer times than the larger particle sizes. Of particular interest at the 50nm liposomes, which could maintain 0.5 μm/s velocity as the cloud approach the limits of the field of view. This indicates that smaller, more flexible particles can reach larger distances within a shorter time during a parenchymal infusion.

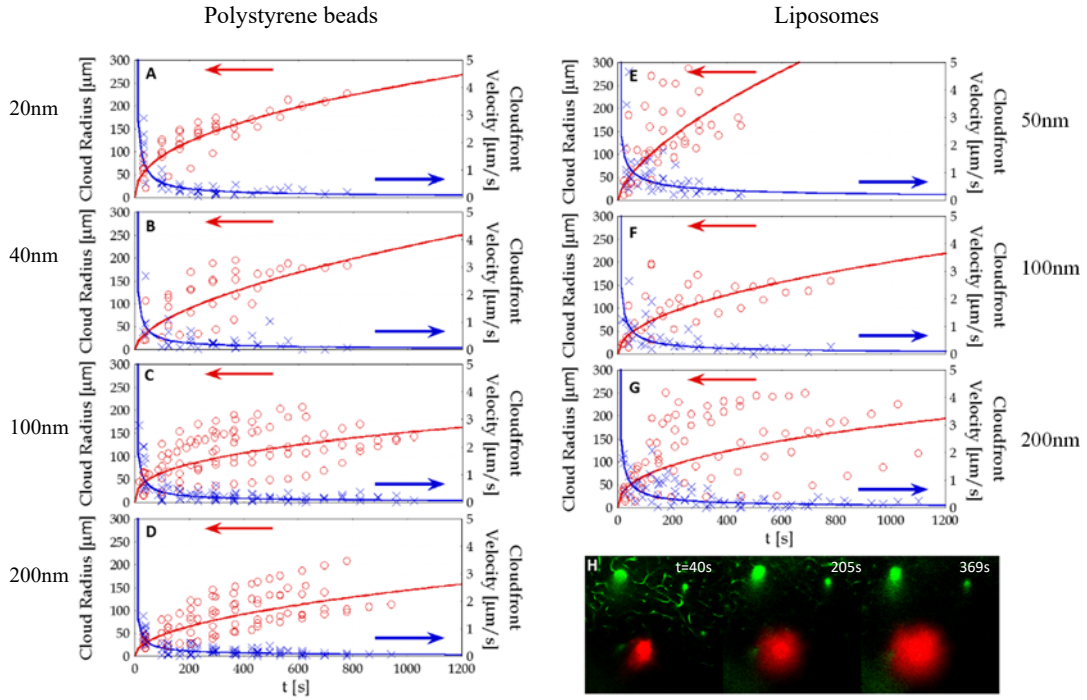

Figure 6.5. Increasing cloud radius and decreasing cloud wavefront velocities were compared for each particle size and type. (A) to (D) Polystyrene beads sized 20 and 40nm exhibited higher radial growth over time than 100 nm and 200 nm. In the right column, (E) to (G) shows liposomes, where 50nm exhibited significantly higher cloud radius over time than any other particle (H) Time lapse images of radial cloud growth at the needle plane for 20nm particles, 250 µm beneath the surface of the brain.

6.4.5 Perivascular spaces are more preferential as high conductance fluid pathways

The perivascular space provide an alternative route of high-conductance fluid route for particles passing though the ECS as shown in Figure 6.6 for 100nm nanoparticles. Depending on the size of the particle and PVS width, the particle experiences limited hindrance to its movement, adopting fluid movement in the PVS. This change in transport modality leads to the anisotropy in the cloud shape, as shown in Figure 6.1. From figure 6.7 PVS parameters are plotted against each other based particles on size and type. In figure 6.7 (b) width of each PVS involved in the infusion

cloud is measured. We found that an overwhelming majority of vessels visualized in the infusion do not have their perivascular spaces occupied by particles. Within the network of capillaries, arterioles/venuoles, and arteries/veins, only 1-6 vessels displayed accessible PVS. Figure 6.7 (a) shows the majority of vessels with accessible PVS were below 20 μm. This is partially due to where we infused, which was generally 100 to 300 μm below the cortical surface. The nearest available PVS would likely be along a capillary. Figure 6.7 (b) shows the majority of PVS widths are between 1 and 10 μm. In Figure 6.7 (c), we show PVS width vs. vessel diameter. For the measured vessels, the width of the annulus surrounding the vessels is of similar size to the diameter of the vessel in most cases.

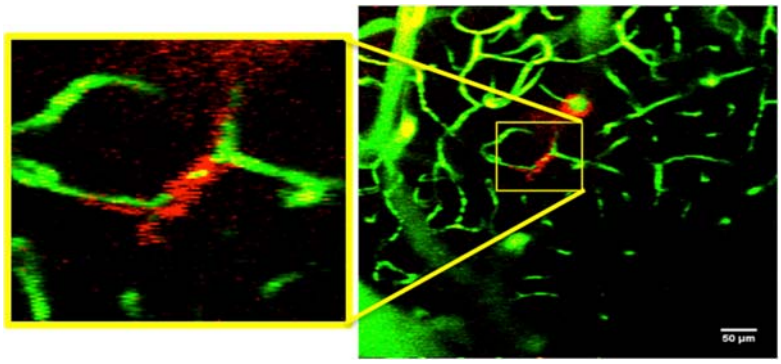

Figure 6.6 Inset of 100nm nanoparticle (red) preferential flow along the perivascular spaces of the blood vessels (FITC green). The depth of infusion source - needle is at 80um depth from in the rat cortex from the surface.

There are a few cases of smaller vessels having PVS 1.5 times the size of the vessel, and a few cases of larger vessels having PVS 0.5 to 0.25 times the size of the vessel. In addition, the annulus of surrounding the vessel, in a large proportion of the vessels, was not completely regular surrounding the vessel. This is likely due to unique

anatomy in the neurovascular unit. Differences in this anatomy compared to unavailable PVS in other local vessels could be indicators of why particular PVS are available to be entered by the particles, but were beyond the scope of our experiments. Figures 6.7 (d) and (f) display various comparisons of the PVS velocities. Figure 6.7 (d) shows the average PVS velocity with standard error of the mean for each particle size. The liposomes, to the left of the dividing line, show roughly the same average PVS velocity as the beads on the right of the line. The averages all fall between 6-7 μm/s, with the exception of the 50 nm liposomes, which averaged to about 9.2 μm/s. A larger proportion of the 50 nm liposomes had higher measured PVS velocity than those seen with the other particle sizes. Sample sizes starting from left at 50 nm liposomes, to right ending at 200 nm beads, were n = 29, 12, 26, 28, 18, 26, 28 respectively. Figure 6.7 (e) plots PVS velocity vs. distance of the PVS entrance from the needle outlet. At this low flow rate, there does not seem to be any discernable effect of the pressure gradient on PVS velocity, as the majority of the velocities for all distances measured falls between 3 and 12 μm/s. Figure 6.7 (f) shows the PVS velocity vs. PVS width. Again, there does not seem to be any trend within this data. The majority of the measured PVS widths fall between 1 and 10 μm, and the velocities are between 3 and 12 μm/s. The 50 nm liposome data can be seen to be somewhat higher for a number of the points, influencing the higher average velocity seen in Figure 6.7 (d).

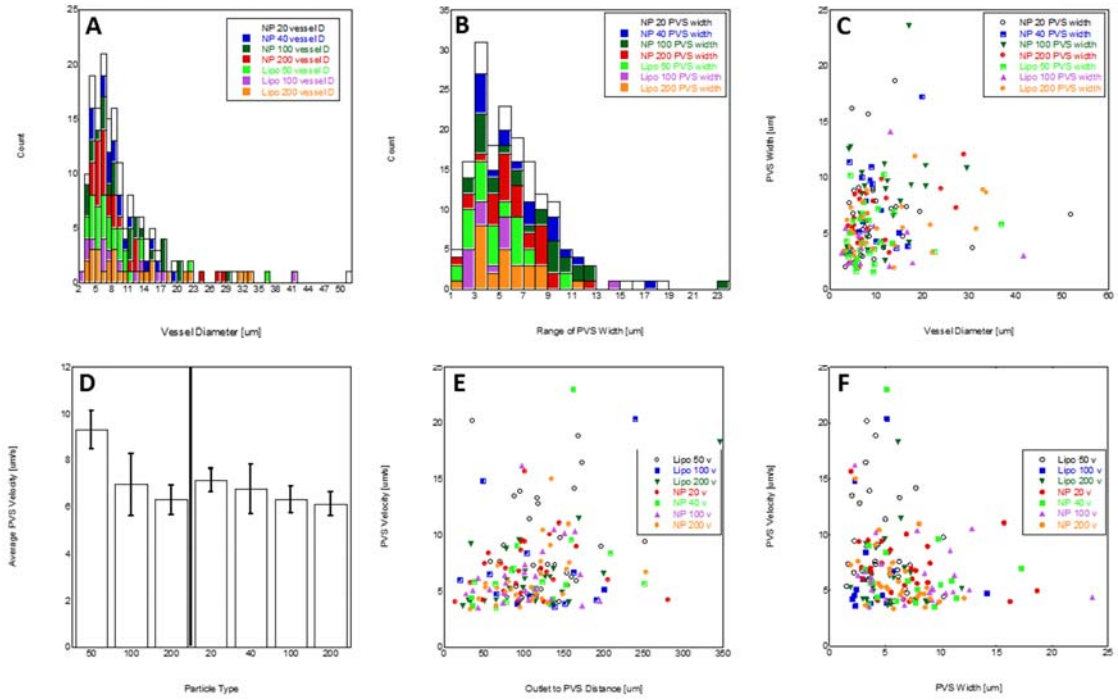

Figure 6.7 Perivascular spaces are more preferential as high conductance fluid pathways. (A) and (B) Number of PVS routes were plotted against their manually measured blood vessel diameters and PVS widths. On an average, (C) PVS were about the same size as the vessel there were surrounding. (D) Average PVS velocities for liposomes were relatively larger than nanoparticles. (E) and (F) PVS velocity were compared against outlet to PVS distance and PVS width. Smaller particles were capable of having higher velocities at larger distances from the needle outlet.

6.4.6 Volume of distribution for larger nanoparticles is greatly influenced by perivascular spaces.

Perivascular spaces play a vital role in drug delivery, specifically when drug particle size is close to or exceeds the size of ECS pores. We calculated the distance between the needle outlet and PVS entry point for each route taken along the blood vessels. Figure 6.8 (a) shows the measured PVS volumes in relation to distance from the needle outlet. We do not see any significant relation in the distance travelled from the outlet needle to the volume occupied, as the majority of the PVS volumes are below

0.0002 μL for any distance from the needle outlet. Following this, we looked at the relationship between PVS volume and its width as shown in Figure 6.8 (b). There is a trend among the data, but it is strongly influenced on how the perivascular volume is calculated as infused volume and calculated volume can vary. Next, we calculated cumulative PVS volume as a fraction of the total volume (combined cumulative parenchymal and perivascular volume). This gives us a better idea of the partitioning of the particles across the time of infusion, for each of the particle types and sizes. In Figure 6.8 (c), we show the average ratio of PVS volume to total volume across all times for each particle type. On the left of the dividing line, the liposomes range from about 10% to 20% PVS volume to total volume. On the right of the line, the beads range from about 5% to 20% PVS volume to total volume. Interestingly, the liposomes do not display a trend, and 100 nm liposomes seem significantly higher than the other two liposome sizes. This can be attributed to the absence or presence of large number of observed PVS during these infusions. A higher proportion had higher PVS volume relative to the total volume, which can be seen in Figure 6.8 (d). Here, all individual data points of PVS volume could be compared directly to the total volume for a given sample. The smaller particles (50 nm liposomes and 20 nm beads) have smaller values for the PVS volume to total volume ratio, which is consistent with what is seen during the infusion. This is further shown in Figure 6.8 (e), where cumulative PVS volume to total volume ration drops over time. For the first few minutes in the infusions, it is possible for all of the particles sizes to have between 20% and 80% of the total volume occupied in the local PVS. With time there is a decrease in the PVS volume relative to total volume

across all of the particle sizes but at different rates. Smaller 50 nm liposomes and 20 nm beads (blue), drop off much quicker than the other particles.

Due to the slower parenchymal velocity of the larger particles, the PVS to total volume ratio can stay between 1% and 10% past the 10 minute mark in some of the infusions for the 100 nm liposomes, and 100 and 200 nm beads. Figure 6.8 (f) shows that the PVS volume becomes significantly less than the cloud volume at longer times. Altogether, this analysis demonstrates the relative effect local PVS exerts on infusion. PVS volume fraction decreases faster for smaller particle sizes indicating greater PVS influence on larger sizes.

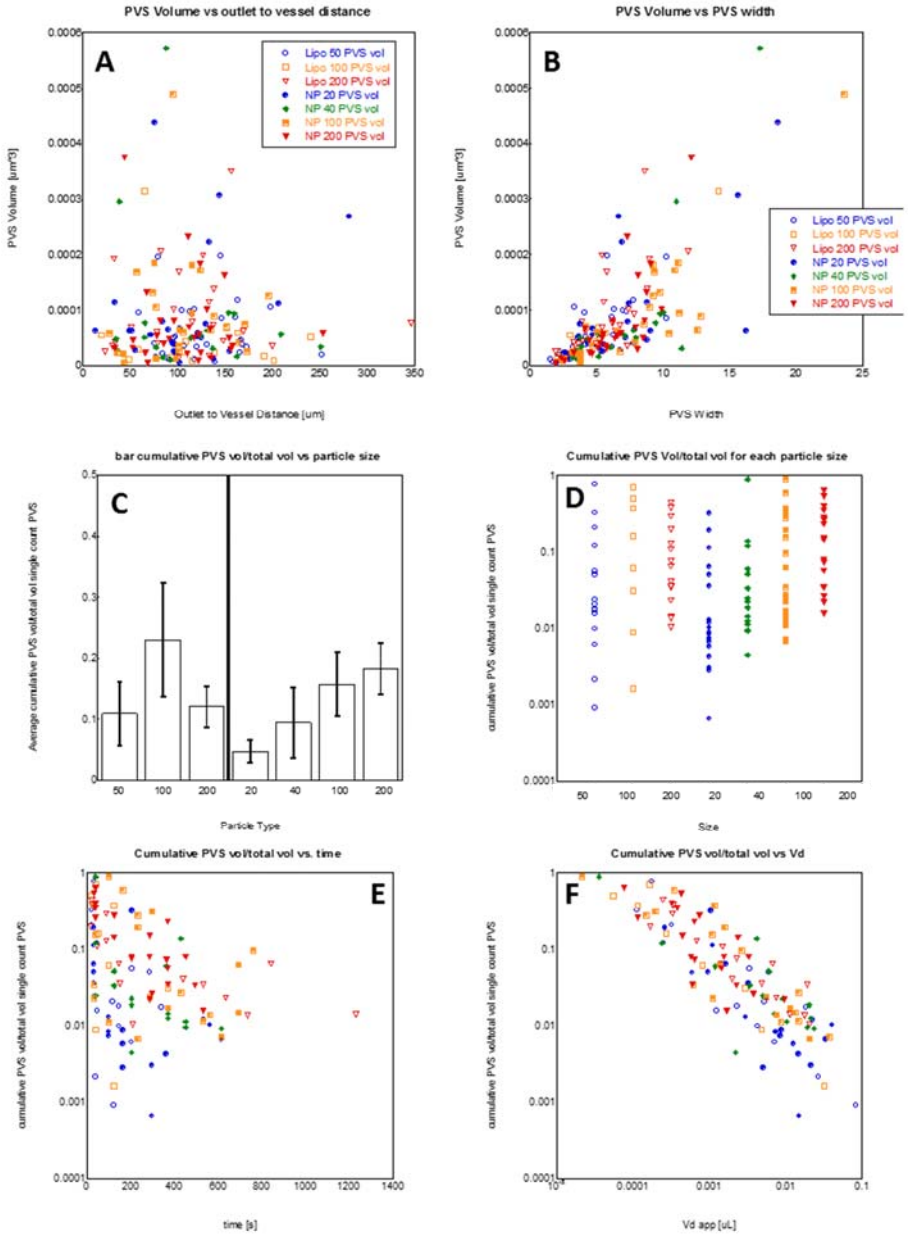

Figure 6.8 Volume of distribution for larger nanoparticles is greatly influenced by perivascular spaces. (A) Distance from needle outlet to PVS entry point was compared against cumulative PVS volume. Volumes ranged up to 10^{-4}µl. (B) Width of the perivascular spaces is compared against cumulative PVS volume. (C) and (D) Cumulative PVS volume as a fraction of total volume for liposomes (to the left of central line) and nanoparticles (to the right of central line). For nanoparticles, it increase with size, whereas for flexible liposomes, it varies with access or density of perivascular spaces. (E) and (F) Cumulative PVS volume as a fraction of total volume is compared against time and total volume of distribution. Smaller particle sizes had larger distribution volumes in shorter times.

6.4.7 Co-Infusion of smaller and larger particles into rat cortex

To observe hindered and unhindered transport at the same time through rat cortex, we co-infused a smaller molecule (Cascade Blue dextran 3kDa) with large sized 200 nm polystyrene beads and imaged under custom made 4-channel two photon microscope. Figure 6.9 shows dual infusion from the needle tip, smaller molecules (blue) occupy significantly larger volumes in comparison the 200nm sized nanoparticles (red). This reiterates the role played by ECS pores, where 3 kDa particles, which are relatively larger compared to saline molecules, face limited to zero resistance in the parenchyma. The initial fluid velocity of the Cascade Blue dextran is estimated to be ~4.8 μm/s, which can be a factor of 10 to 100 times greater than the movement of the beads, depending on their distance from the infusion point. We are restricted here by field of view of the microscope and expect the smaller particles to proliferate much further into the parenchyma.

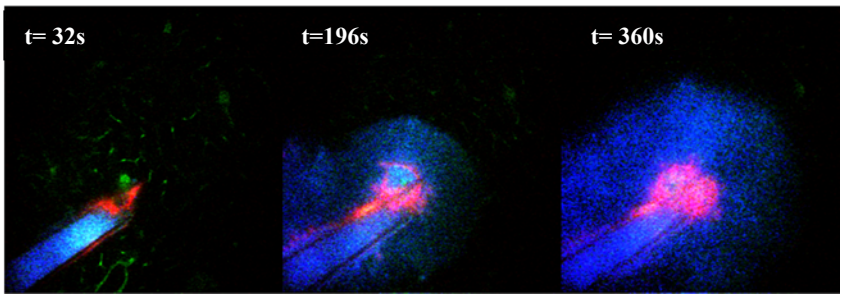

Figure 6.9 Co-infusion of small and large particles by CED in rat cortex. The needle outlet was placed about 200 μm below the surface of the brain and co infused with small particles of 3kDa Cascade Blue dextran (blue) and 200 nm polystyrene beads (red) at 0.2ul/min infusion rate. Smaller particles have a larger volume of distribution than larger particles.

6.5 DISCUSSION AND CONCLUSION

Currently, monitoring and understanding convection enhanced drug delivery *in vivo* is limited by the imaging modality used in clinical trials, MRI. Current clinical trials with convection enhanced drug delivery in the brain have not been entirely successful. The failure of clinical trials like the PRECISE [20]–[22], reinforced the need to understand the transport dynamics better inside the brain. Advancing therapeutic treatments for diseases like glioblastoma where gliomas proliferate along the PVS, makes targeting the PVS more crucial. In this paper, we observed that on increasing infused particle size more than ECS pore size, volume occupied by particles in PVS increased relative to parenchymal volume at the same depth in the brain. Many studies have worked on increases the total volume of distribution [28]–[30] in the parenchyma, however there is a need to develop targeted therapeutics for perivascular spaces to have better clinical outcomes.

Former studies in this field have been done with MRI and recently real time MRI has been demonstrated with maximum frame rate of 50 frames/s and resolution of 1.5 x 1.5 x 8 mm^3 [23]. However, very few studies have attempted volumetric or 3-dimensional imaging [31]–[33]. We used a 3-dimensional volumetric imaging system with two-photon excitation fluorescence microscopy at frame rate of 3.15 frames/s and resolution of 1.1 x 1.1 x 2 μm^3, for an infusate flow rate of 0.2µl/min. We captured transport dynamics in real time at different planes that is at the source and about 200-250µm around it. This kind of real time imaging visualizes dynamics of drug infusion

in micrometer scale resolution, allowing for better estimation of real occupied volume. In particular, we were able to image the anisotropy and isotropy in the infusion cloud determined by convection, diffusion, particle size, and specifically presence of perivascular spaces near infusion.

We observed that infusion cloud is heavily influences by presence of local PVS, this is attributed to higher CSF convective currents [11][34] in the CSF that provide a high conductance fluid pathway. Diem et al., estimated fluid PVS velocity to be about 8.33 μm/s [13], [35], but Foley et al., determined it to be about 25 μm/s [27]. In our studies with real time volumetric imaging, we determined particles velocities in the range of 3-23 μm/s, thus encompassing all values determined in previous studies. We were also able to see the range of the PVS velocities, and estimate them in a more precise method.

For more flexible and smaller nanoparticles, the infusion cloud is isotropic. Anisotropy is more apparent in larger particles, 100 nm and 200 nm nanoparticles, and is directly correlated with the presence of perivascular spaces near the point of infusion.

In the parenchyma, particles move slower and their velocity drops with time as show in Figure 6.7. For most infusions, parenchymal velocities of the cloud front start around 0.5-3 μm/s and then drop to velocities around 0.01-0.5 μm/s over time. We can estimate that when infusions reach a certain distance away from the needle (~100 μm), the nanoparticles moving in the PVS can move two or more orders of magnitude *faster*

than nanoparticles in the ECS for the infusion rate of 0.2 μL/min used in these experiments..

In co-infusion experiments, we chose the 200 nm sized beads, for they experienced maximum hindrance to their movement whereas cascade blue dextran molecules had unhindered fluid like motion. We also observed that velocity of the particles drops significantly with increasing distance from outlet of the infusion needle and an increase in infusion rate does not affect penetration distance over time. These contribute towards limiting penetration distance of larger particles for clinical purposes.

Though we have high spatial and temporal resolution, the limitation with this system is imaging deep inside the brain and capture the infusate distribution in those regions. Hence, we have calculated the relative volume of distribution within an area of 573 x 573 um in a single plane above the needle plane. Volume of distribution to volume of infusion ratio (Vd/Vi) is indicative of effective targeted volume for a given infusion. Zhou et al. used PLGA nanoparticles of mean size 71 nm ± 13 nm and 147 nm ± 27 nm to get Vd/Vi ratio of 3.7 ± 0.3 for trehalose coated particles, and 0.6 ± 0.1 for standard PLGA particles [30], imaged by PET and post-mortem by fluorescence imaging. In contrast, we used high resolution real time volumetric two-photon imaging and got average Vd/Vi values between ~0.01 and 0.02. This is indicative of particles being extremely hindered on entering the brain tissue, and occupy roughly $1/10^{th}$ the volume of a smaller nanoparticle infused in a similar manner. Flexibility of the particle plays a crucial role in increasing the volume distribution as they it aids in maneuvering

through tight ECS spaces. We observed that liposomes of all sizes were able to occupy a larger volume of distribution than the beads for any size. Developing liposomes of different sizes and rigidity, gives more options make targeted treatments to parenchyma and perivascular spaces.

In conclusion, we have imaged at micron resolution and captured the transport dynamics of convection enhanced nanoparticle and liposome delivery in a rat cortex, and quantified the transport dynamics in the perivascular and parenchymal regions. Real time imaging of particle transport in the rat cortex has led to a better understanding of movement of materials that have been infused directly into brain tissue during a CED infusion. These findings particularly the variation in the PVS velocities and parenchymal velocities based on particle size and blood vessels size open the door to a better understanding of drug infusion studies in the brain and parameters that underlie it. By changing parameters, movement of the infused particles can be altered, thus allowing for better control for potential clinical design and optimization. Future studies using this technique will enable better prediction and optimization of convection enhanced drug delivery in clinical trials.

REFERENCES

[1] N. U. Barua, S. S. Gill, and S. Love, “Convection-Enhanced Drug Delivery to the Brain: Therapeutic Potential and Neuropathological Considerations,” *Brain Pathol.*, vol. 24, no. 2, pp. 117–127, 2013.

[2] C. Johanson, “Choroid Plexus–Cerebrospinal Fluid Circulatory Dynamics: Impact on Brain Growth, Metabolism, and Repair,” in *Neuroscience in Medicine*, P. M. Conn, Ed. Totowa, NJ: Humana Press, 2008, pp. 173–200.

[3] N. A. Jessen, A. S. F. Munk, I. Lundgaard, and M. Nedergaard, “The Glymphatic System: A Beginner’s Guide,” *Neurochem. Res.*, vol. 40, no. 12, pp. 2583–2599, 2015.

[4] J. J. Iliff *et al.*, “A paravascular pathway facilitates CSF flow through the brain parenchyma and the clearance of interstitial solutes, including amyloid β.,” *Sci. Transl. Med.*, vol. 4, no. 147, p. 147ra111, Aug. 2012.

[5] R. G. Thorne and C. Nicholson, “In vivo diffusion analysis with quantum dots and dextrans predicts the width of brain extracellular space.,” *Proc. Natl. Acad. Sci. U. S. A.*, vol. 103, no. 14, pp. 5567–72, Apr. 2006.

[6] M. T. Krauze *et al.*, “Effects of the perivascular space on convection-enhanced delivery of liposomes in primate putamen.,” *Exp. Neurol.*, vol. 196, no. 1, pp. 104–11, Nov. 2005.

[7] G. Xi *et al.*, “Convection-enhanced delivery of nanodiamond drug delivery platforms for intracranial tumor treatment.,” *Nanomedicine*, vol. 10, no. 2, pp. 381–91, Feb. 2014.

[8] V. Varenika, A. P. Kells, F. Valles, P. Hadaczek, J. Forsayeth, and K. S. Bankiewicz, “Controlled dissemination of AAV vectors in the primate brain.,” *Prog. Brain Res.*, vol. 175, pp. 163–72, Jan. 2009.

[9] V. A. Cuddapah, S. Robel, S. Watkins, and H. Sontheimer, “A neurocentric perspective on glioma invasion.,” *Nat. Rev. Neurosci.*, vol. 15, no. 7, pp. 455–65, Jul. 2014.

[10] E. T. Zhang, H. K. Richards, S. Kida, and R. O. Weller, “Directional and compartmentalised drainage of interstitial fluid and cerebrospinal fluid from the rat brain.,” *Acta Neuropathol.*, vol. 83, no. 3, pp. 233–9, Jan. 1992.

[11] M. L. Rennels, T. F. Gregory, O. R. Blaumanis, K. Fujimoto, and P. A. Grady, “Evidence for a ‘Paravascular’ fluid circulation in the mammalian central nervous system, provided by the rapid distribution of tracer protein throughout the brain from the subarachnoid space,” *Brain Res.*, vol. 326, no. 1, pp. 47–63, Feb. 1985.

[12] M. L. Rennels, O. R. Blaumanis, and P. A. Grady, “Rapid solute transport throughout the brain via paravascular fluid pathways.,” *Adv. Neurol.*, vol. 52, pp. 431–9, Jan. 1990.

[13] R. O. Carare *et al.*, “Solutes, but not cells, drain from the brain parenchyma along basement membranes of capillaries and arteries: significance for cerebral amyloid angiopathy and neuroimmunology.,” *Neuropathol. Appl. Neurobiol.*, vol. 34, no. 2, pp. 131–44, Apr. 2008.

[14] P. Hadaczek *et al.*, "The 'perivascular pump' driven by arterial pulsation is a powerful mechanism for the distribution of therapeutic molecules within the brain.," *Mol. Ther.*, vol. 14, no. 1, pp. 69–78, Jul. 2006.

[15] P. Wang and W. L. Olbricht, "Fluid mechanics in the perivascular space.," *J. Theor. Biol.*, vol. 274, no. 1, pp. 52–7, Apr. 2011.

[16] V. Kiviniemi *et al.*, "Ultra-fast magnetic resonance encephalography of physiological brain activity - Glymphatic pulsation mechanisms?," *J. Cereb. Blood Flow Metab.*, p. 0271678X15622047, Dec. 2015.

[17] et al. Westphal M, Hilt DC, Bortey E, Delavault P, Olivares R, Warnke PC, "A phase 3 trial of local che- motherapy with biodegradable carmustine (BCNU) wafers (Gliadel wafers) in patients with primary malignant glioma," *Neuro Oncol.*, 2003.

[18] R. H. Bobo, D. W. Laske, A. Akbasak, P. F. Morrison, R. L. Dedrick, and E. H. Oldfield, "Convection-enhanced delivery of macromolecules in the brain.," *Proc. Natl. Acad. Sci. U. S. A.*, vol. 91, no. 6, pp. 2076–80, Mar. 1994.

[19] P. F. Morrison, M. Y. Chen, R. S. Chadwick, R. R. Lonser, and E. H. Oldfield, "Focal delivery during direct infusion to brain: role of flow rate, catheter diameter, and tissue mechanics," *Am J Physiol Regul. Integr. Comp Physiol*, vol. 277, no. 4, pp. R1218-1229, Oct. 1999.

[20] J. H. Sampson *et al.*, "Poor drug distribution as a possible explanation for the results of the PRECISE trial.," *J. Neurosurg.*, vol. 113, no. 2, pp. 301–9, Aug. 2010.

[21] S. R. Husain, B. H. Joshi, and R. K. Puri, “Interleukin-13 receptor as a unique target for anti-glioblastoma therapy.,” *Int. J. Cancer*, vol. 92, no. 2, pp. 168–75, Apr. 2001.

[22] D. W. Laske, O. Ilercil, A. Akbasak, R. J. Youle, and E. H. Oldfield, “Efficacy of direct intratumoral therapy with targeted protein toxins for solid human gliomas in nude mice.,” *J. Neurosurg.*, vol. 80, no. 3, pp. 520–6, Mar. 1994.

[23] R. Saito *et al.*, “Gadolinium-loaded liposomes allow for real-time magnetic resonance imaging of convection-enhanced delivery in the primate brain.,” *Exp. Neurol.*, vol. 196, no. 2, pp. 381–9, Dec. 2005.

[24] F. Gimenez *et al.*, “Image-guided convection-enhanced delivery of GDNF protein into monkey putamen.,” *Neuroimage*, vol. 54 Suppl 1, pp. S189-95, Jan. 2011.

[25] R. M. Richardson *et al.*, “Interventional MRI-guided putaminal delivery of AAV2-GDNF for a planned clinical trial in Parkinson’s disease.,” *Mol. Ther.*, vol. 19, no. 6, pp. 1048–57, Jun. 2011.

[26] C. Mamot *et al.*, “Extensive Distribution of Liposomes in Rodent Brains and Brain Tumors Following Convection-Enhanced Delivery,” *J. Neurooncol.*, vol. 68, no. 1, pp. 1–9, May 2004.

[27] C. P. Foley, N. Nishimura, K. B. Neeves, C. B. Schaffer, and W. L. Olbricht, “Real-time imaging of perivascular transport of nanoparticles during convection-enhanced delivery in the rat cortex.,” *Ann. Biomed. Eng.*, vol. 40, no. 2, pp. 292–303, Feb. 2012.

[28] J. A. MacKay, D. F. Deen, and F. C. Szoka, “Distribution in brain of liposomes after convection enhanced delivery; modulation by particle charge, particle diameter, and presence of steric coating.,” *Brain Res.*, vol. 1035, no. 2, pp. 139–53, Feb. 2005.

[29] K. B. Neeves, A. J. Sawyer, C. P. Foley, W. M. Saltzman, and W. L. Olbricht, “Dilation and degradation of the brain extracellular matrix enhances penetration of infused polymer nanoparticles.,” *Brain Res.*, vol. 1180, pp. 121–32, Nov. 2007.

[30] J. Zhou *et al.*, “Highly penetrative, drug-loaded nanocarriers improve treatment of glioblastoma.,” *Proc. Natl. Acad. Sci. U. S. A.*, vol. 110, pp. 11751–6, 2013.

[31] G. Gholyhu and W. R. Wkh, “ClearPoint MRI guided devices CED into brain _ fierce druf delivery,” vol. 6, pp. 6–8, 2013.

[32] K. Sillay *et al.*, “Convection enhanced delivery to the Brain: preparing for gene therapy and protein delivery to the Brain for functional and restorative Neurosurgery by understanding low-flow neurocatheter infusions using the Alaris(®) system infusion pump.,” *Ann. Neurosci.*, vol. 20, no. 2, pp. 52–8, Apr. 2013.

[33] E. Lueshen, M. LaRiviere, B. Yamini, and A. Linninger, “Computer simulations and in vivo convection-enhanced delivery of fluorescent nanoparticles demonstrate variable distribution geometry,” *Comput. Chem. Eng.*, vol. 71, pp. 672–676, Dec. 2014.

[34] J. J. Iliff *et al.*, "Impairment of Glymphatic Pathway Function Promotes Tau Pathology after Traumatic Brain Injury," *J. Neurosci.*, vol. 34, no. 49, pp. 16180–16193, Dec. 2014.

[35] A. K. Diem *et al.*, "A Simulation Model of Periarterial Clearance of Amyloid-β from the Brain," *Front. Aging Neurosci.*, vol. 8, p. 18, Feb. 2016.

[36] L. Shi *et al.*, "Quantification of transient increase of the blood – brain barrier permeability to macromolecules by optimized focused ultrasound combined with microbubbles," *Int. J. Nanomedicine*, pp. 4437–4448, 2014.

[37] F. Wang *et al.*, "Targeted Delivery of GDNF through the Blood-Brain Barrier by MRI-Guided Focused Ultrasound," *PLoS One*, vol. 7, no. 12, pp. 1–8, 2012.

CHAPTER 7

CONCLUSION AND FUTURE DIRECTIONS

Novel nonlinear optical imaging techniques earlier used for micromachining and developed for *in vitro* applications have the potential to be a powerful technique for single cell genetic manipulation. The work done in this dissertation develops this technique further and integrates it with custom built two-photon microscope systems. In this final chapter, we review the conclusions and future directions presented on the various topics here.

The ability to manipulate a single cell using regenerative amplifier based 1kHz systems with 2- 3 pulses and low average power has been explored more in this dissertation. We characterize the biophysical properties in more depth before it could be applied to *in vivo* systems. We studied the role of calcium in optopotation experiments under different concentrations. Resealing time significantly decreases across 0 mM to 10 mM extracellular calcium concentrations. We expanded on the model for membrane pore dynamics and were able to fit perforation kinetics under different calcium concentrations to the same model. Additionally we studied inflow of different sized dextrans to support the same model. Based on this work, we can say that pore resealing and successful transfection are dependent on calcium concentrations in the extracellular and intracellular solution. Pore resealing dynamics were quantified on the model that fit both our inflow and outflow experiments. All these together set the stage for *in vivo* experiments.

We took this work further and established a working model for successful *in vivo* single cell optoporation. The parameter and dynamics we explored were in good

agreement with in vitro optoporation experiments. We successfully showed inflow and outflow experiments in a single cell in the cortex of an anesthetized mouse. This approach is however highly dependent on user skill. For future experiments, there is potential to explore transfection in neurons with naked DNA plasmids that do not induce an immune response, siRNA and quantum dots. Moreover, co-labeling other components of the cell will aid in visualizing the process of optoporation *in vivo* in more detail. This opens up opportunities to study other neurological diseases such as tumor initiation, propagation or failure from a single cell. It has the potential to study cell- cell functionality in normal and diseased tissues alone and in combination with other technologies, including three photon imaging, optogenetics, hyperspectral imaging and transgenic animals.

In this dissertation, we also studied Convection Enhanced Drug delivery integrating it with real time volumetric two-photon imaging. Generally MRI's are employed in clinical trials but they do not explore transport dynamics at micrometer resolution. Here we have captured and analyzed transport dynamics of convection enhanced delivery of rigid polystyrene beads in the range of 20nm to 200nm and flexible liposomes in the range of 50nm to 200nm. We demonstrate the major role played by perivascular spaces in volume of distribution for small, large and flexible particles. Small flexible particles have higher volume of distribution than large rigid particles, which in turn prefer perivascular routes more. This works sets the stage to create custom designed and targeted CED systems based on disease proliferation. It also expands our understanding of CED for predicting optimal needle placement and estimating infusate

distribution based on vasculature and tissue environment.

Lastly, the ability to manipulate and study biological systems *in vivo* can help advance our understanding of diseases at a single cell level and also at a macro level by designing better clinical trials. This work lays the groundwork for future *in vivo* experiments for both single cell optoporation and CED pre-clinical trials.